The Astrophysical Journal, 838:41 (21pp), 2017 March 20 https://doi.org/10.3847/1538-4357/aa63f9

The Most Massive Active Galactic Nuclei at $1 \lesssim z \lesssim 2$

Hyunsung D. Jun[1,2,3], Myungshin Im[2], Dohyeong Kim[2], and Daniel Stern[1]
[1] Jet Propulsion Laboratory, California Institute of Technology, 4800 Oak Grove Drive, Pasadena, CA 91109, USA; hyunsung.jun@jpl.nasa.gov
[2] Center for the Exploration of the Origin of the Universe (CEOU), Astronomy Program, Department of Physics and Astronomy, Seoul National University, Seoul 151-742, Korea; mim@astro.snu.ac.kr
Received 2016 October 27; revised 2017 February 17; accepted 2017 February 20; published 2017 March 22

Abstract

We obtained near-infrared spectra of 26 Sloan Digital Sky Survey quasars at $0.7 < z < 2.5$ with reported rest-frame ultraviolet $M_{\rm BH} \sim 10^{10}\,M_{\odot}$ to critically examine the systematic effects involved with their mass estimations. We find that active galactic nuclei (AGNs) heavier than $10^{10}\,M_{\odot}$ often display double-peaked Hα emission, extremely broad Fe II complex emission around Mg II, and highly blueshifted and broadened C IV emission. The weight of this evidence, combined with previous studies, cautions against the use of $M_{\rm BH}$ values based on any emission line with a width over 8000 km s^{-1}. Also, the $M_{\rm BH}$ estimations are not positively biased by the presence of ionized narrow line outflows, anisotropic radiation, or the use of line FWHM instead of σ for our sample, and unbiased with variability, scatter in broad line equivalent width, or obscuration for general type-1 quasars. Removing the systematically uncertain $M_{\rm BH}$ values, $\sim 10^{10}\,M_{\odot}$ black holes (BHs) in $1 \lesssim z \lesssim 2$ AGNs can still be explained by anisotropic motion of the broad line region from $\sim 10^{9.5}\,M_{\odot}$ BHs, although current observations support that they are intrinsically most massive, and overmassive to the host's bulge mass.

Key words: galaxies: active – galaxies: evolution – quasars: supermassive black holes

Supporting material: data behind figure

1. Introduction

Since the identification of supermassive black holes (BHs) at the center of galaxies, their typical mass ($M_{\rm BH}$) values have been measured in the $10^{6-9}\,M_{\odot}$ range (e.g., Kormendy & Richstone 1995). The more recent discovery of $\sim 10^{10}\,M_{\odot}$ BHs (McConnell et al. 2011) in quiescent galaxies further extended the mass limit, pushing the previous $\sim 10^{9}\,M_{\odot}$ boundary to heavier regimes. These extremely massive BHs ($>10^{9.5}\,M_{\odot}$, hereafter EMBHs) give constraints to how massive a BH can grow through accretion within the inner galaxy (e.g., Inayoshi & Haiman 2016; King 2016). Also, the EMBHs are thought to reside in $\sim 10^{12}\,M_{\odot}$ giant elliptical host galaxies lying on the present-day $M_{\rm BH}$–σ_{*} relation (e.g., Ferrarese & Merritt 2000; Gebhardt et al. 2000), though we note there are exceptions to the expectation that BH growth closely follows that of the host (e.g., van den Bosch et al. 2012; Seth et al. 2014; Walsh et al. 2015).

Direct evidence for the existence of $10^{10}\,M_{\odot}$ BHs was initially reported in a handful of nearby quiescent galaxies (e.g., NGC 3842 and NGC 4889, McConnell et al. 2011; NGC 1277, van den Bosch et al. 2012), albeit with the validity of some of the measurements being questioned (Emsellem 2013). Even if we consider that the measured values are acceptable, the EMBHs tend to lie above the $M_{\rm BH}$–σ_{*} or, more frequently, the $M_{\rm BH}$–$L_{\rm bulge}$ relations extrapolated from lower-mass BHs (e.g., Gültekin et al. 2009; Kormendy & Ho 2013), by up to an order of magnitude (see also Savorgnan & Graham 2016 on measurement issues for $L_{\rm bulge}$). To explain the high mass of EMBHs with respect to their host galaxies, Volonteri & Ciotti (2013) suggest that EMBHs are formed through frequent dry mergers. However, this does not solve the problem entirely because such mergers might not necessarily induce strong active galactic nucleus (AGN) activity in EMBHs found up to at least $z = 5$ (e.g., Jun et al. 2015, hereafter J15; Wu et al. 2015).

These observational and theoretical considerations lead to the natural question of whether the estimates of $M_{\rm BH} \sim 10^{10}\,M_{\odot}$ in AGNs are reliable. The $M_{\rm BH}$ estimators applied to high-redshift quasar spectra have mainly relied on UV-based spectral features that are secondarily calibrated to hydrogen Balmer line-based estimators. One possibility is that the UV-based $M_{\rm BH}$ values are overestimated somehow. Independent $M_{\rm BH}$ estimates from Balmer line-based estimators would enhance the reliability of $10^{10}\,M_{\odot}$ BHs in distant quasars. Unfortunately, direct comparison between the UV-based versus Balmer-based $M_{\rm BH}$ estimates has been scarce for EMBHs. Previous studies have been largely limited to $M_{\rm BH} < 10^{9.5}\,M_{\odot}$ (e.g., Netzer et al. 2007; Shang et al. 2007; Dietrich et al. 2009; Greene et al. 2010; Ho et al. 2012; Park et al. 2013), and such studies are controversial regarding the scatter between C IV and Balmer-based estimators while consistent on the agreement betwen Mg II and Balmer-based $M_{\rm BH}$ values. The most extensive study in this respect was done by Shen & Liu (2012, hereafter S12) where the sample includes dozens of EMBHs, though with few BHs above $10^{10}\,M_{\odot}$.

In order to understand the mass growth of EMBHs, accurate $M_{\rm BH}$ measurements over a range of redshifts is vital. In the distant universe, however, direct dynamical measurement of $M_{\rm BH}$ becomes difficult for quiescent galaxies, as it is hard to resolve the gravitational sphere of influence from the BH. Instead, broad line gas kinematics are used to estimate the $M_{\rm BH}$ of AGNs, where this method gives more uncertain results. $M_{\rm BH}$ measurements for AGNs are based on the reverberation mapping technique (Blandford & McKee 1982; Peterson 1993) which measures the time delay of the broad line emission to the incident continuum and thus estimates the size of the broad line region ($R_{\rm BLR}$). The $R_{\rm BLR}$ values for Hβ are further calibrated by

[3] NASA Postdoctoral Program Fellow.

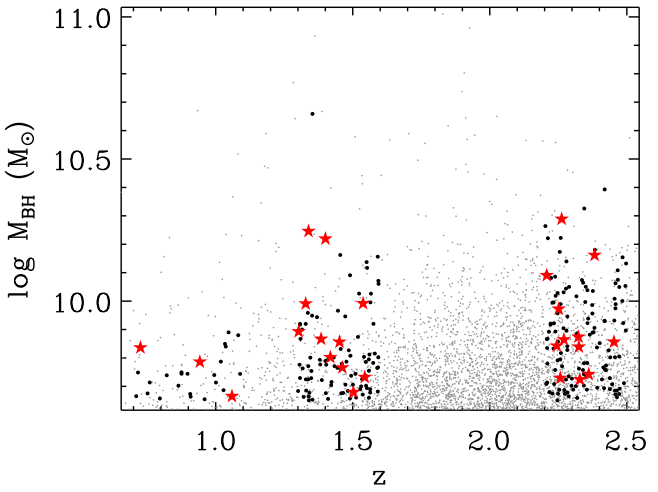

Figure 1. Distribution of the massive end $M_{\rm BH}$ values at intermediate redshifts, with the measurements from Shen et al. (2011, gray dots). Those within our redshift and sensitivity cuts, flagged or visually inspected for spurious line profiles or fitting, are displayed (black circles), among which we selected 26 for IRTF follow-up spectroscopy (red stars).

the radius–luminosity relationship ($R_{\rm BLR}$–L relation, Kaspi et al. 2000; Bentz et al. 2006), which allows the estimation of $M_{\rm BH}$ from a single-epoch measurement of optical continuum/line luminosity and broad line width.

High-redshift AGNs have their rest-frame optical (rest-optical) emission redshifted to the infrared, and their rest-frame ultraviolet (rest-UV) emission redshifted into the optical. The single-epoch mass estimators are thus secondarily calibrated in the UV assuming that the UV continuum luminosity and broad emission line (C IV or Mg II) widths follow the optical $R_{\rm BLR}$–L relation and optical line widths respectively, as a linear or power-law relation. Ongoing studies tentatively find that the slope of the C IV $R_{\rm BLR}$–L relation follows that of the optical relation, and extends up to the most luminous quasars (Kaspi et al. 2007; Sluse et al. 2011; Chelouche et al. 2012). However, the UV continuum luminosities and line widths are not tightly correlated with the optical quantities, introducing an intrinsic scatter of ∼0.4 dex when comparing C IV and Balmer $M_{\rm BH}$ measurements (e.g., J15).

In addition to the issues regarding the reliability of the rest-UV $M_{\rm BH}$ measurements, the rest-optical $M_{\rm BH}$ measurement from single-epoch spectroscopy itself has limitations on its accuracy due to the systematic uncertainties in deriving the mass equation. Bearing in mind that the single-epoch $M_{\rm BH}$ values have sizeable errors from the poorly constrained constant (virial factor, hereafter f-factor) in the mass equation (0.3–0.4 dex systematic uncertainty, e.g., Kormendy & Ho 2013; McConnell & Ma 2013) and the $R_{\rm BLR}$–L relation (0.1–0.2 dex intrinsic scatter, Bentz et al. 2013), it is possible that the $M_{\rm BH}$ values of the most extreme AGNs could have been biased to high values if they were selected to have outlying f-factors or $R_{\rm BLR}$ values with respect to the calibrations. Indeed, theoretical and technical issues that could positively bias the $M_{\rm BH}$ measurements have been reported, from accretion disk modeling (Laor & Davis 2011; Wang et al. 2014) or profile fit methodology (Peterson et al. 2004; Collin et al. 2006). Furthermore, potential limitations of automated spectral fitting of a large sample of spectra failing to model unusual spectral features (e.g., Shen et al. 2008), or using single-epoch spectroscopy to derive representative AGN properties, should be carefully checked, especially at extreme mass values.

In this paper, we present rest-optical spectra of 26 quasars at $0.7 < z < 2.5$ with UV-based $\sim 10^{10}\,M_\odot$ $M_{\rm BH}$ measurements, obtained with the NASA Infrared Telescope Facility (IRTF). We aim to double check the consistency of the massive end UV–optical $M_{\rm BH}$ estimates, and examine if the measurements could be systematically biased to unusually high masses from spectral features and during application of the mass estimator. We describe the sample selection and data acquisition of extremely massive AGNs (Section 2), the spectral analysis in determining $M_{\rm BH}$ (Section 3), the results (Section 4) and implications on the measured $M_{\rm BH}$ values (Section 5). Throughout, we adopt a flat ΛCDM cosmology with $H_0 = 70$ km s^{-1} Mpc^{-1}, $\Omega_m = 0.3$, and $\Omega_\Lambda = 0.7$ (e.g., Im et al. 1997).

2. Data

2.1. Sample Description and Observations

We selected the extremely massive AGN sample from the Sloan Digital Sky Survey (SDSS) type-1 quasar catalog (DR7, Schneider et al. 2010). The spectral fitting results and the $M_{\rm BH}$ estimates in Shen et al. (2011) were adopted for target selection, using the Hβ line at $z < 0.8$, Mg II at $0.8 < z < 2.0$, and C IV at $z > 2.0$. We identified the sample by applying the following selection criteria:

1. Mass selection of $M_{\rm BH} \geqslant 5 \times 10^9\,M_\odot$
2. Redshift cut of $0.7 < z < 2.5$ to place the broad Hα and Hβ lines within the near-infrared (NIR) spectroscopic windows, excluding redshifts where both Hα and Hβ are close to NIR telluric absorption ($1.1 < z < 1.3$ and $1.6 < z < 2.2$)
3. Continuum signal-to-noise ratio (S/N) cut of 20 or higher from the SDSS spectra for good line width and flux measurements, H-band magnitude <17.8 AB mag, bright enough for IRTF observations
4. Removal of objects flagged or visually inspected to show double-peaked Hβ lines, severely absorbed Mg II or C IV, and obvious mismatch between the model and the spectrum

yielding 1254 quasars sufficing the $M_{\rm BH}$ and redshift cut, and 261 objects with further sensitivity limits and flags, among which we arbitrarily selected 26 objects spanning the optical continuum luminosities[4] of $L_{5100} = 10^{45.7\text{–}47.2}$ erg s^{-1}, for IRTF observations. Figure 1 shows the redshift–$M_{\rm BH}$ distribution of our sample.

We used the SpeX instrument (Rayner et al. 2003) on the IRTF to obtain the NIR spectra of the targets. The 0.8–2.4 μm cross-dispersed mode (SXD) was chosen, with a slit width of 0.″8 or 1.″6 depending on the seeing conditions. This yields a spectral resolution of $R = 750$ or 375 throughout the observed wavelengths, which is tuned for sensitivity over resolution for the broad AGN emission lines and continuum features. The exposure times for the targets were aimed to give a continuum S/N per resolution element of at least 10 around Hβ, and 5 around Hα. We carefully checked each field to avoid neighbor

[4] Throughout this paper we use subscript numbers on the monochromatic luminosity to indicate its wavelength, such as $L_{5100} = L$(5100 Å).

Table 1
Summary of IRTF Observations

Name	Coordinates	z	H	t_{exp}	R
J0102+00	J010205.89+001157.0	0.727	16.85	30	750
J1010+05	J100943.56+052953.9	0.944	17.07	9	375
J0748+22	J074815.44+220059.5	1.060	16.10	24	750
J0840+23	J083937.85+223940.7	1.312	16.25	18	750
J1057+31	J105705.16+311907.9	1.329	17.30	24	750
J0203+13	J020256.11+124928.0	1.352	17.49	30	750
J0319–07	J031926.24–072808.8	1.391	16.78	30	375
J1053+34	J105250.06+335504.9	1.414	16.40	12	750
J1035+45	J103453.06+445723.2	1.424	15.25	9	750
J1055+28	J105440.84+273306.4	1.453	17.12	18	750
J0146–10	J014542.78–100807.7	1.465	16.76	24	750
J0400–07	J040022.40–064928.6	1.516	16.58	30	375
J0855+05	J085515.59+045232.8	1.541	17.08	18	750
J0741+32	J074043.47+314201.2	1.546	17.70	24	750
J1522+52	J152156.48+520238.6	2.221	15.44	6	750
J1339+11	J133928.39+105503.2	2.250	17.18	12	750
J0905+24	J090444.34+233354.1	2.258	16.62	30	750
J0257+00	J025644.69+001246.0	2.264	17.78	30	750
J2123–01	J212329.47–005052.9	2.282	15.90	12	750
J0052+01	J005202.41+010129.2	2.283	17.07	18	750
J2112+00	J211157.78+002457.5	2.335	17.58	36	375
J1027+30	J102648.16+295410.9	2.349	16.92	24	750
J0651+38	J065101.23+380759.6	2.355	17.75	30	375
J1036+11	J103546.03+110546.5	2.368	16.45	18	750
J0752+43	J075158.65+424522.9	2.466	17.64	24	375
J0946+28	J094602.31+274407.1	2.476	16.66	18	750

Note. z is the redshift of the Hα line (Section 3), H is the H-band AB magnitude, t_{exp} is the total exposure time in minutes, and R is the spectral resolution.

source contamination when nodding the spectrum along the 15″ slit length. The observations were performed during three full and three half nights in 2011 December, 2012 February/December along with another program, summing to a total on-source integration of 9.3 hr for all the targets (0.1–0.6 hr per target). The weather conditions were overall photometric but atmospheric seeing varied from 0.6–2″. We nodded the spectra in AB mode with a 90–180 s frame time for good dark and sky subtraction, and observed A0 V type standard stars near to the target for telluric absorption correction (Vacca et al. 2003) and flux calibration. Also, a set of flat-field and argon arc wavelength calibration data were taken. We summarize the IRTF observations in Table 1.

In addition to the NIR spectroscopy, we compiled the optical spectra of quasars from the SDSS database (DR12 including both the SDSS-I/SDSS-II and the SDSS-III BOSS data, Alam et al. 2015) in order to calculate the M_{BH} values from C IV and Mg II lines and to compare them with masses from hydrogen Balmer lines or previous rest-UV measurements. Also, broad-band photometric data from *GALEX* GR7, SDSS DR12, 2MASS PSC, UKIDSS DR10, and *WISE* AllWISE releases (Martin et al. 2005; Skrutskie et al. 2006; Lawrence et al. 2007; Wright et al. 2010; Alam et al. 2015) were collected to supplement the spectra with monochromatic continuum luminosities. The latest spectra (SDSS-III BOSS over SDSS-I/SDSS-II) and photometry (UKIDSS over 2MASS) were used when the target had overlapping data, while multiple spectra from the same instrument were averaged.

2.2. Data Reduction

We reduced the IRTF spectra using the IDL-based package Spextool (version 3.4, Cushing et al. 2004). It involves pre-processing (linearity, flat correction), spectral extraction, wavelength and flux calibration, combining multiple spectral frames, telluric correction, order merging, and spectrum cleaning. The standard package configuration was adopted, with a seeing-dependent, 0.7–1.″2 Gaussian spatial extraction radius set equal for the target and standard star spectra. We found up to a ∼10%–20% level of flux difference at overlaps between different orders of the cross-dispersed spectra, which were leveled using the Spextool package. Moreover, we checked the accuracy of standard star flux calibration by convolving each flux-calibrated IRTF spectrum by the broad SDSS/UKIRT filter response curves, and comparing the spectroscopic flux to that from the photometry. Overall, we find the mean and rms scatter of the spectroscopic to photometric flux ratio to be 0.97 ± 0.36 when averaged over the set of *griz* filters (not taking into account the *u*-band because the shortest-wavelength cutoff is different for the photometry and the spectroscopy), and 0.91 ± 0.35 for the *YJHK* filters. In order to reduce the scatter between the spectral and photometric fluxes, we linearly interpolated the flux ratios and gave multiplicative corrections to the SDSS and IRTF spectra, where the mean and rms scatter of the spectroscopic to photometric flux ratio change to 1.00 ± 0.00 and 1.01 ± 0.07 for the *griz* and *YJHK* bands, respectively.

We plot the flux-calibrated spectra together with the photometric data points in Figure 2. The SDSS and IRTF spectra meet fairly well at their boundaries though the short-wavelength (∼1 μm) IRTF data are noisy due to some of the data being taken in bright lunar phases and the weaker sensitivity of higher-order spectra. The average and 1-σ scatter of the continuum S/N[5] are 89 ± 30 and 15 ± 11 for the SDSS and IRTF spectra, suitable for measuring M_{BH} for most of the targets except for some from the Hβ line. We applied Galactic extinction corrections assuming the total-to-selective extinction ratio of $R_V = 3.1$ and the $E(B-V)$ values from Bonifacio et al. (2000) that revised the values in the Schlegel et al. (1998) extinction map.

3. Analysis

In order to estimate the single-epoch M_{BH} values from Hβ, Hα, Mg II, C III], and C IV lines, we fit the broad line regions from the joint SDSS/IRTF spectra.[6] We start from the rest-frame 4200–5600 Å fit around Hβ for which we used a power-law for the continuum, broad Fe II component, and broad and narrow Gaussian components for the line. After fitting the power-law continuum determined by 4100–4300 and 5500–5700 Å windows and subtracting it from the spectrum, we determined the width (FWHM = 900–20,000 km s^{-1}) and height of the Fe II complex using the Boroson & Green (1992) template while iteratively updating the continuum. We utilized the 4450–4650 and 5150–5350 Å regions to derive the height and the full fitting range to obtain the width of the Fe II, through a least chi-squares fit to the continuum subtracted spectrum. The Hβ emission was fit by a single narrow (full width at half

[5] Throughout this paper we measure the S/N per wavelength element $\Delta\lambda = \lambda/750$ unless quoting the numbers from references.

[6] Throughout, we used the IDL-based package MPFIT (Markwardt 2009) for all least-squares fitting unless stated otherwise.

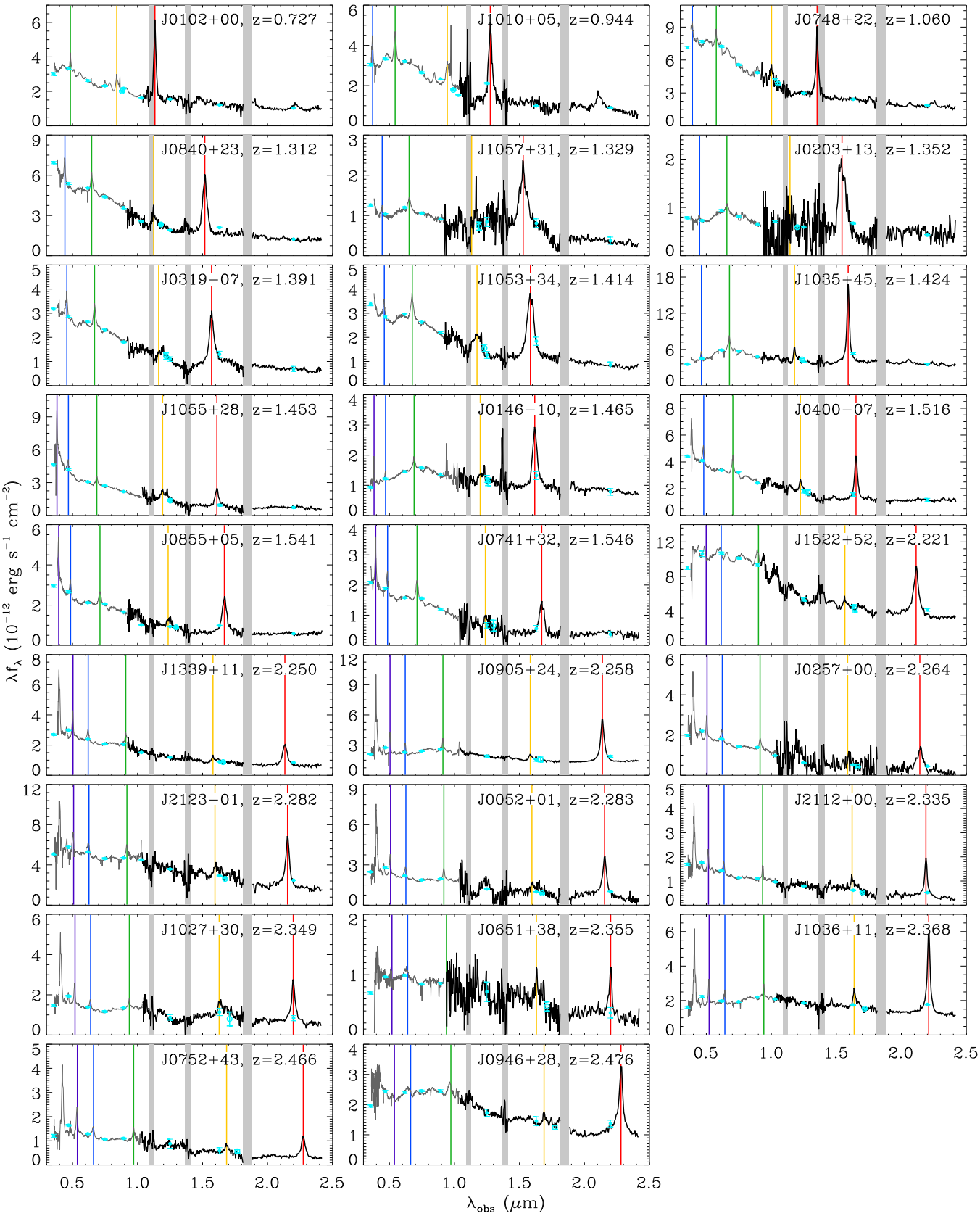

Figure 2. Reduced observed-frame SDSS (gray) and IRTF (black) spectra of the sample, binned to $R \sim 400$ for display purposes. Gray shaded regions are wavelengths with strong NIR telluric absorption. The photometric data points from SDSS, 2MASS, or UKIDSS are overplotted (filled cyan circles), together with the rest-frame 5100 Å continuum fluxes (open cyan circles). The Hα, Hβ, Mg II, C III], and C IV emission lines are marked in thin red, yellow, green, blue, and purple lines, respectively. The data used to create this figure are available.

maximum, or FWHM $< 1000\,\mathrm{km\,s^{-1}}$ hereafter[7]) Gaussian and double broad (FWHM $= 2000$–$15{,}000\,\mathrm{km\,s^{-1}}$ hereafter) Gaussian components, double narrow Gaussians for each [O III] λ4957, 5007 doublet, and Hγ by a single narrow and single broad Gaussian. When some of the [O III] profiles were broader than their limit, the FWHM limit was relaxed to FWHM $< 2000\,\mathrm{km\,s^{-1}}$. To obtain a better quality fit, we used a common redshift for the narrow Hβ, one of the double narrow [O III]λ4957 and one of the double narrow [O III]λ5007, one of the double broad Hβ, and also the broad and narrow Hγ, while leaving the rest of the components' redshift free. In addition, the centers of each Gaussian component were constrained to lie within $1000\,\mathrm{km\,s^{-1}}$ of the Hα redshift. We masked out or slightly modified the fitting range to exclude noisy regions that yielded a poor initial fit, and removed the fits where S/N < 5. We obtained the monochromatic luminosity L_{5100} and its error from the best-fit model to the spectra with S/N > 5. At S/N < 5 we fit the photometric magnitudes at rest-frame 3000–10,000 Å by a power-law continuum, correcting for the Hα line contribution using the *JHK* filter response curves and the best-fit model to the Hα spectra, to obtain L_{5100} depicted in Figure 2.

Next, we fit the rest-frame 6000–7100 Å region including the Hα emission. We fixed the height and width of the Fe II complex from the Hβ region (or the Mg II region when S/N < 5) since they are weaker and harder to constrain around the Hα emission. A power-law continuum, single narrow Gaussian and double broad Gaussians for the Hα, single narrow Gaussian for each [O I]λ6300, 6364, [N II]λ6548, 6583, and [S II]λ6716, 6731 doublet, were simultaneously fitted to the Fe II subtracted spectrum. We used the width of the [O III] λ5007 from the Hβ fit to fix the width of the crowded assembly of narrow [O I] doublet, [N II] doublet, Hα singlet, and [S II] doublet emission. When the [O III] width was not reliably measured due to poor resolution/sensitivity, we used the mean FWHM of the narrow Hα, $400\,\mathrm{km\,s^{-1}}$, out of $z < 0.37$, S/N > 20 SDSS quasars from Shen et al. (2011). The relative strengths of the narrow [O I], [N II], and [S II] lines were fixed to the values from Vanden Berk et al. (2001). The centers of the narrow lines and one of the double broad Hα components were tied to the same redshift. Also, the centers of every component were restricted to within $1000\,\mathrm{km\,s^{-1}}$ of the Hα redshift, which was determined by the peak of the broad Hα model profile.

We notice that some objects show double-peaked features on top of the smooth, broad Hα, exhibiting relatively wide line widths (FWHM $\gtrsim 8000\,\mathrm{km\,s^{-1}}$) when fitted all together (Section 4.2.1). They resemble the disk emitters explained by a rotating accretion disk source pronounced in a small fraction of Hα spectra, where the broad line luminosity or width using the full profile can overestimate the contribution from the BLR (e.g., Figure 1 in Chen & Halpern 1989; Figure 4 in Eracleous & Halpern 1994). In order to quantify which sources are likely disk emitters, we modeled again the broad Hα spectra using a three-component profile: one signal broad Gaussian, assumed to be the profile from the random motion of the BLR, and double broad Gaussians centered blue- and redward from the Hα redshift by more than $2000\,\mathrm{km\,s^{-1}}$ which we assume to be the rotating disk emitter components. We define an emission line to be double-peaked when non-zero blue- and redshifted broad Gaussian components make up more than half of the total broad Hα luminosity, the triple component model is favored over the single or double component fit with a statistically smaller reduced chi-square (a F-distribution probability of over 0.99), and the disk emitter components are clearly detached in order to distinguish from a simple wide and non-Gaussian BLR model. The criteria give seven classified double-peaked emitters.[8]

Third, we fit the rest-frame 2200–3100 Å region surrounding the Mg II emission. We used the Fe II template from Tsuzuki et al. (2006) because it provides data closer to the center of the Mg II emssion than Vestergaard & Wilkes (2001). Following a methodology similar to the Hβ fitting, we iteratively subtracted the continuum and Fe II complex before fitting the Mg II, determined through 2150–2250 and 3050–3150 Å windows for the continuum, 2150–2410, 2460–2700, and 2900–3150 Å windows for the Fe II height, and the full fitting range for the Fe II width. Afterward, we fitted the Mg II emission with double broad Gaussians and the [Ne IV]/Fe III near 2420–2440 Å with a single broad Gaussian. We required the centers of the Mg II and [Ne IV]/Fe III model components to lie within $1000\,\mathrm{km\,s^{-1}}$ of the Hα redshift, with exceptions for J0946+28 and J1522 +52 where the Mg II centers are blueshifted by more and relaxed to lie between -3000 and $1000\,\mathrm{km\,s^{-1}}$. The Mg II spectra showing absorption features, discontinuity between the SDSS/IRTF spectra, or imperfect Fe II subtraction, were masked or adjusted in the fitting range. We derived L_{3000} and its error from the best-fit model to the Mg II region.

Lastly, we fit the rest-frame 1445–1705 Å region around the C IV emission. When the C IV was unavailable or severely absorbed, we fit the rest-frame 1670–2050 Å region around C III] to use the FWHM as a surrogate to that of C IV (S12). We fixed the height and width of the Fe II complex from those nearby the Mg II because this feature is weaker around the C IV and C III]. We used a power-law continuum and double broad Gaussians for the C IV and C III]. For the C IV region we used single broad Gaussians to fit the 1600 Å feature (Laor et al. 1994), and the blended He II and O III] emission around 1650 Å. For the C III] region we used single broad Gaussians to model each of N IVλ1718, N III]λ1750, Fe IIλ1786 (UV191), Si IIλ1816, Al IIIλ1857, and Si III]λ1891. We masked or changed the fitting range of the C IV/C III] spectra showing strong absorption features, and clipped the spectra showing weaker absorption features by redoing the fit after removing the data below 2.5-σ from the fit. We found the C III] centers to lie between -2000 and $1000\,\mathrm{km\,s^{-1}}$ of the Hα redshift, but C IV is often more blueshifted, so its centers were set between -8000 and $2000\,\mathrm{km\,s^{-1}}$. Depending on the spectral coverage, either L_{1350} or L_{1450} was calculated based on their similarity (Vestergaard & Peterson 2006) as is expected from the small lever arm between them. When the 1350 Å was available we computed the error-weighted average of the 1340–1360 Å fluxes, and if only 1450 Å was covered, the 1440–1460 Å fluxes were used as an approximate measure of L_{1350}. When neither was available, we extrapolated the continuum and Fe II emission from the C III] fit down to 1450 Å while propagating the errors from the fit.

[7] All the line widths mentioned in this paper are corrected for instrumental resolution, e.g., $400\,\mathrm{km\,s^{-1}}$ for $R = 750$ and $800\,\mathrm{km\,s^{-1}}$ for $R = 375$.

[8] We note that our criteria indicate, but do not verify with highly sensitive spectra or sophistcated modeling, that these sources are disk emitters; thus we use the term double-peaked emitter throughout. These Hα based double-peaked emitters are likely to be similar in their properties to the Hβ based double-peaked emitters that we did not include in our sample (Section 2.1). However, we kept them in our analysis to see how they affect M_{BH} estimates.

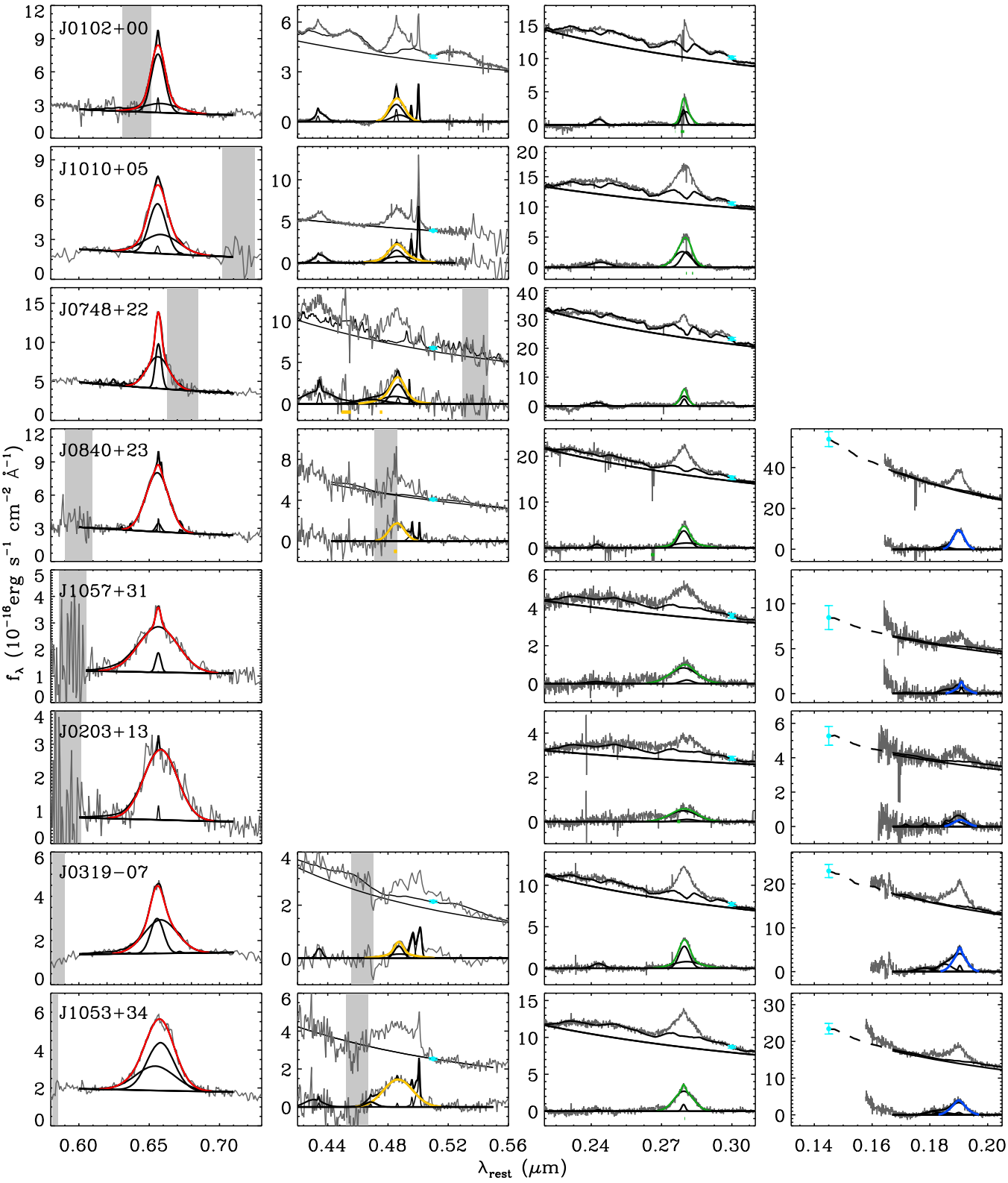

Figure 3. Spectral fitting of Hα, Hβ, Mg II, and C IV or C III] line regions (from left to right). Five spectra with S/N < 5 near the Hβ, one with a large discontinuity between the SDSS/IRTF data near the Mg II, and three without C IV or C III] coverage, are omitted. On top of the resolution-matched spectra are the model narrow lines (thin black), broad lines (thick black lines for individual broad components, colored for the sum of the broad compoments used to derive $M_{\rm BH}$), the continuum (black line in the upper spectrum), the Fe II complex (black curve on top of the continuum), and the sum of the total line components (black line in the lower spectrum). Masked regions are highlighted below the lower spectrum (thick lines colored identical to the broad emission), and the monochromatic luminosities, L_{5100}, L_{3000}, L_{1350}/L_{1450} on the upper spectrum (cyan dots). Extrapolations to the L_{1350}/L_{1450} are shown (black dashed line).

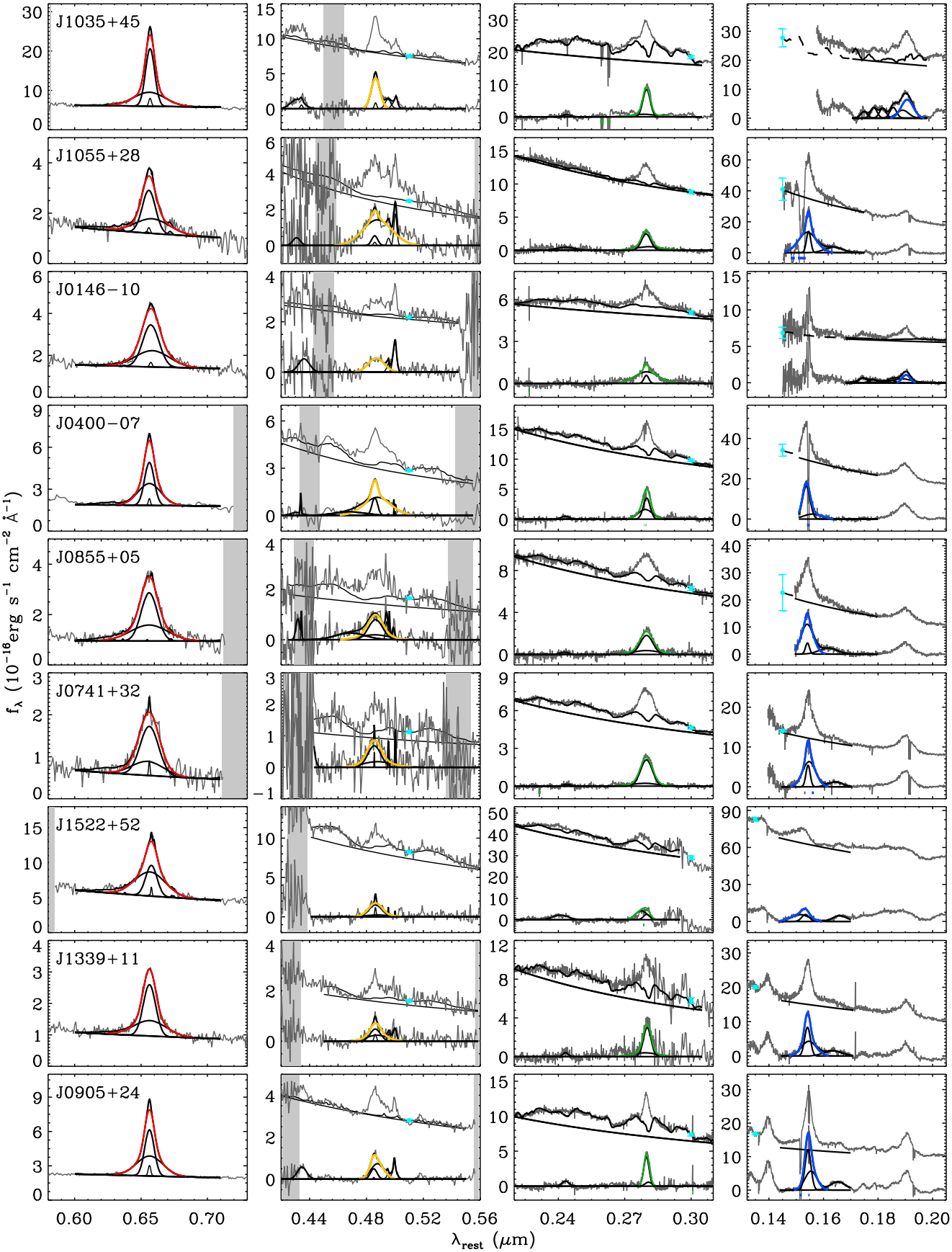

Figure 3. (Continued.)

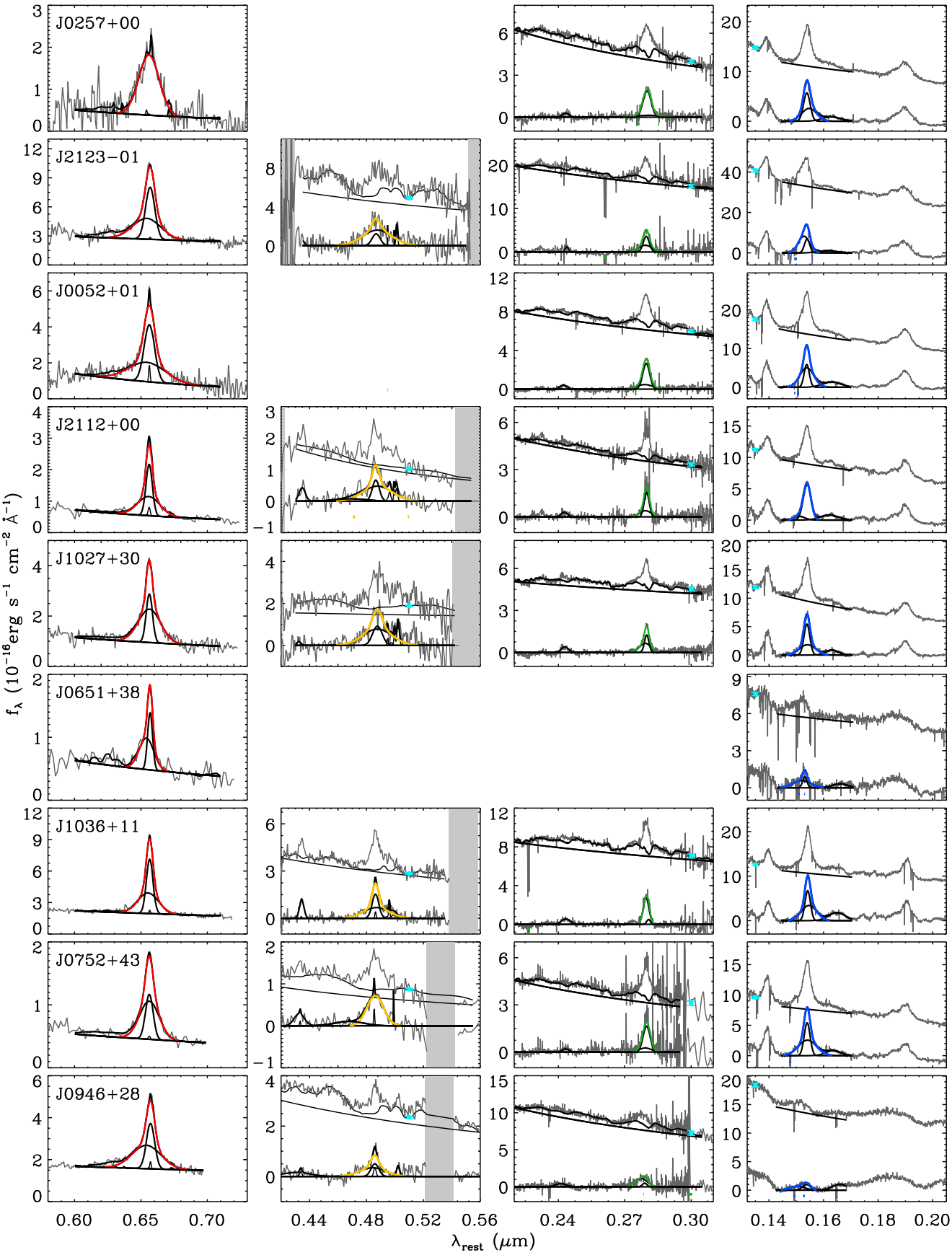

Figure 3. (Continued.)

Table 2
Emission Line Properties

Name	$v_{\mathrm{H}\alpha} - v_{\mathrm{C\,IV}}$	$\mathrm{FWHM}_{\mathrm{C\,III]/IV}}$	$\mathrm{FWHM}_{\mathrm{Mg\,II}}$	$\mathrm{FWHM}_{\mathrm{H}\beta}$	$\mathrm{FWHM}_{\mathrm{H}\alpha}$	$\sigma_{\mathrm{C\,III]/IV}}$	$\sigma_{\mathrm{Mg\,II}}$	$\sigma_{\mathrm{H}\beta}$	$\sigma_{\mathrm{H}\alpha}$
J0102+00	···	···	3726 ± 96	7252 ± 232	5686 ± 273	···	2104 ± 45	3120 ± 85	3186 ± 226
J1010+05	···	···	7653 ± 189	8409 ± 311	<7613	···	3622 ± 81	4938 ± 231	<4152
J0748+22	···	···	3581 ± 357	7528 ± 1091	3401 ± 132	···	1937 ± 142	4612 ± 1032	2890 ± 61
J0840+23	···	7197 ± 367	6963 ± 181	7446 ± 1067	7918 ± 72	3075 ± 52	4560 ± 144	3162 ± 437	3610 ± 21
J1057+31	···	3821 ± 474	13063 ± 3082	···	<10464	3298 ± 371	6159 ± 1567	···	<5797
J0203+13	···	8594 ± 609	14053 ± 6015	···	<12747	3649 ± 176	6181 ± 2662	···	<4983
J0319-07	···	6805 ± 199	6687 ± 119	5176 ± 1033	7431 ± 297	3652 ± 81	4598 ± 97	4628 ± 907	4522 ± 140
J1053+34	···	8566 ± 663	7910 ± 136	14037 ± 633	<11628	4066 ± 159	4263 ± 65	5960 ± 271	<5129
J1035+45	···	8159 ± 200	4372 ± 56	4496 ± 166	4279 ± 44	3465 ± 69	3205 ± 15	1909 ± 61	3697 ± 74
J1055+28	652 ± 74	6266 ± 220	5895 ± 241	11164 ± 5447	<6381	5703 ± 234	4237 ± 453	6156 ± 3235	<3730
J0146-10	···	5150 ± 261	6831 ± 225	8139 ± 881	7789 ± 338	2187 ± 93	5389 ± 128	3456 ± 361	4205 ± 234
J0400-07	2007 ± 81	6818 ± 89	4747 ± 153	5551 ± 312	4851 ± 203	4413 ± 71	2719 ± 141	5214 ± 220	3016 ± 154
J0855+05	1430 ± 76	7832 ± 354	7914 ± 291	8051 ± 1060	7549 ± 245	4217 ± 167	4322 ± 299	4469 ± 1088	4164 ± 137
J0741+32	642 ± 109	6175 ± 134	7139 ± 118	7586 ± 1008	<8281	4210 ± 75	3823 ± 123	4524 ± 857	<3598
J1522+52	6028 ± 131	10546 ± 819	6862 ± 436	7099 ± 982	6514 ± 144	5948 ± 553	2859 ± 126	3650 ± 1503	4317 ± 80
J1339+11	1255 ± 46	6214 ± 205	4706 ± 209	6365 ± 2192	5871 ± 222	4187 ± 242	3626 ± 230	3689 ± 1854	3704 ± 231
J0905+24	677 ± 16	6183 ± 100	3164 ± 97	5529 ± 256	4782 ± 41	3506 ± 85	1393 ± 54	2659 ± 96	3456 ± 42
J0257+00	1543 ± 171	6813 ± 147	4771 ± 113	···	<8191	4181 ± 178	3103 ± 212	···	<3142
J2123-01	2244 ± 51	7282 ± 125	4123 ± 230	8006 ± 1362	4649 ± 119	3745 ± 62	2476 ± 247	5844 ± 1262	3510 ± 106
J0052+01	1961 ± 44	6327 ± 93	4255 ± 157	···	5179 ± 174	4258 ± 74	2511 ± 324	···	4048 ± 105
J2112+00	1859 ± 28	6724 ± 103	3232 ± 181	5336 ± 725	3117 ± 113	3394 ± 106	2006 ± 258	5334 ± 702	2814 ± 110
J1027+30	1846 ± 39	5868 ± 159	3265 ± 193	7394 ± 900	3686 ± 139	4212 ± 289	2177 ± 160	5508 ± 854	3029 ± 87
J0651+38	3651 ± 90	5393 ± 275	···	···	2593 ± 180	5394 ± 270	···	···	1952 ± 87
J1036+11	1236 ± 23	5915 ± 127	3412 ± 90	4433 ± 422	3299 ± 55	4342 ± 155	1399 ± 30	4250 ± 471	2632 ± 58
J0752+43	1700 ± 47	6379 ± 68	4211 ± 178	8517 ± 684	4379 ± 338	5052 ± 74	2040 ± 257	3617 ± 269	2722 ± 152
J0946+28	5320 ± 225	11172 ± 1870	5901 ± 536	5666 ± 735	4459 ± 92	5584 ± 635	2769 ± 189	4738 ± 453	3881 ± 74

Note. The C IV to Hα broad line shift (positive for blueshifted C IV, km s^{-1}) and the line widths (FWHM and σ, in km s^{-1}). The C III] line widths are used instead of the C IV when the C IV line is not covered. Upper limits to the line width values are associated with double-peaked Hα emission.

In Figure 3 we plot the fit to the spectra around the broad emission lines for each object, and in Tables 2 and 3 we summarize the spectral measurements. Once the spectral fitting was performed around each broad line, we derived the broad line FWHM and line dispersion (hereafter σ). The errors on FWHM were determined by equating the FWHM of the combined double Gaussian model as a linear combination of the constituent single Gaussian FWHMs (interpolated or extrapolated, depending on the relative magnitude of the FWHMs), and propagating the errors from each single FWHM measurement. For σ and its error, we used the second moment of the model fit fluxes up to the point they are equal to the flux errors; this corresponds to ±2.0 FWHM from the broad line center on average. Out of the 26 objects in our sample, we compile 21, 26, 25, and 23 line widths from Hβ, Hα, Mg II, and C IV/C III], respectively. We note that some of the broad component's FWHM values are close to the lower limit of 2000 km s^{-1} and are intermediate in width, e.g., Hα in J1057+31 and Mg II in J1053+34. These could be confused with narrow lines with strong outflows, where we test the possible change in the M_{BH} values in Section 4.2.4. Meanwhile, the spectroscopic continuum luminosities are corrected for the photometric calibration uncertainty (∼0.02 mag) involved when scaling the spectra (Section 2.2).

4. Results

4.1. M_{BH} Estimation of Our Sample

The determined continuum luminosities and broad line FWHMs are plugged into single-epoch M_{BH} estimators for AGNs from J15 for each emission line measurement, assuming the constant $f = 5.1 \pm 1.3$ from Woo et al. (2013) and the R_{BLR}–L relation from Bentz et al. (2013)

$$\log\left(\frac{M_{\mathrm{BH}}}{M_{\odot}}\right) = a + \log\left(\frac{f}{5.1}\right) + b\,\log\left(\frac{L}{10^{44}\ \mathrm{erg\ s^{-1}}}\right) + c\,\log\left(\frac{\mathrm{FWHM}}{10^{3}\ \mathrm{km\ s^{-1}}}\right), \quad (1)$$

where (a, b, c) values using the combination of (L, FWHM) below are

$(a, b, c) =$
(L_{5100}, $\mathrm{FWHM}_{\mathrm{H}\beta}$): (6.94 ± 0.12, 0.533 ± 0.034, 2)
(L_{5100}, $\mathrm{FWHM}_{\mathrm{H}\alpha}$): (7.05 ± 0.12, 0.533 ± 0.034, 2.12 ± 0.03)
($100L_{\mathrm{H}\alpha}$, $\mathrm{FWHM}_{\mathrm{H}\alpha}$): (6.72 ± 0.12, 0.511 ± 0.033, 2.12 ± 0.03)
(L_{3000}, $\mathrm{FWHM}_{\mathrm{Mg\,II}}$): (6.62 ± 0.12, 0.548 ± 0.035, 2.45 ± 0.06)
(L_{1350}, $\mathrm{FWHM}_{\mathrm{C\,IV}}$): (6.67 ± 0.15, 0.547 ± 0.037, 2.11 ± 0.11). (2)

Because some of the Balmer lines covered by the IRTF spectra have marginal sensitivity and the Hβ line is a few times weaker than Hα, we compare the intrinsic scatter[9] σ_{int} between the Hα

[9] $\sigma_{\mathrm{int}}^2 = \Sigma_{i=1}^{N}\{(y_i - x_i)^2 - (\Delta x_i^2 + \Delta y_i^2)\}/(N-1)$ for N measurements (x_i, y_i) and errors (Δx_i, Δy_i).

Table 3
Luminosities and M_{BH} Values

Name	log $L_{1350/1450}$	log L_{3000}	log L_{5100}	log $L_{H\alpha}$	$M_{BH,C\ III]/IV}$	$M_{BH,Mg\ II}$	$M_{BH,H\beta}$	$M_{BH,H\alpha}$	Flags
J0102+00	⋯	45.86 ± 0.009	45.68 ± 0.008	44.34 ± 0.042	⋯	9.03 ± 0.14	9.56 ± 0.13	9.53 ± 0.14	⋯
J1010+05	⋯	46.16 ± 0.010	45.95 ± 0.008	44.67 ± 0.052	⋯	9.95 ± 0.16	9.83 ± 0.14	<9.95	DPE
J0748+22	⋯	46.62 ± 0.009	46.32 ± 0.009	44.83 ± 0.025	⋯	9.40 ± 0.19	9.93 ± 0.19	9.40 ± 0.15	⋯
J0840+23	46.91 ± 0.029	46.67 ± 0.010	46.33 ± 0.008	45.06 ± 0.010	10.07 ± 0.21	10.13 ± 0.16	9.93 ± 0.19	10.19 ± 0.14	⋯
J1057+31	46.11 ± 0.068	46.06 ± 0.015	45.89 ± 0.058	44.83 ± 0.014	9.06 ± 0.22	10.46 ± 0.29	⋯	<10.21	DPE, Fe II
J0203+13	45.92 ± 0.045	45.97 ± 0.012	45.81 ± 0.013	44.84 ± 0.023	9.70 ± 0.21	10.49 ± 0.48	⋯	<10.35	DPE, Fe II
J0319-07	46.60 ± 0.029	46.44 ± 0.010	46.11 ± 0.009	44.87 ± 0.033	9.85 ± 0.20	9.96 ± 0.16	9.52 ± 0.22	10.01 ± 0.14	[O III]
J1053+34	46.62 ± 0.027	46.51 ± 0.008	46.20 ± 0.008	45.11 ± 0.054	10.08 ± 0.22	10.17 ± 0.16	10.41 ± 0.14	<10.47	DPE, Fe II
J1035+45	46.70 ± 0.049	46.84 ± 0.010	46.68 ± 0.008	45.46 ± 0.012	10.08 ± 0.21	9.73 ± 0.16	9.67 ± 0.15	9.81 ± 0.15	[O III]
J1055+28	46.90 ± 0.076	46.54 ± 0.012	46.22 ± 0.010	44.73 ± 0.055	9.94 ± 0.21	9.88 ± 0.16	10.27 ± 0.45	<9.93	DPE, [O III]
J0146-10	46.12 ± 0.048	46.31 ± 0.011	46.17 ± 0.008	44.88 ± 0.051	9.34 ± 0.19	9.91 ± 0.16	9.92 ± 0.17	10.09 ± 0.15	Fe II, [O III]
J0400-07	46.86 ± 0.038	46.63 ± 0.009	46.33 ± 0.008	44.96 ± 0.041	10.00 ± 0.21	9.70 ± 0.16	9.68 ± 0.15	9.73 ± 0.15	C IV
J0855+05	46.70 ± 0.128	46.46 ± 0.013	46.11 ± 0.010	44.89 ± 0.031	10.04 ± 0.22	10.15 ± 0.16	9.87 ± 0.18	10.02 ± 0.14	⋯
J0741+32	46.50 ± 0.008	46.33 ± 0.010	45.94 ± 0.014	44.67 ± 0.262	9.71 ± 0.20	9.97 ± 0.16	9.73 ± 0.18	<10.02	DPE
J1522+52	47.61 ± 0.008	47.51 ± 0.013	47.19 ± 0.008	45.74 ± 0.019	10.81 ± 0.24	10.57 ± 0.19	10.34 ± 0.20	10.47 ± 0.16	C IV
J1339+11	47.02 ± 0.008	46.83 ± 0.023	46.50 ± 0.009	45.12 ± 0.040	10.00 ± 0.21	9.80 ± 0.17	9.88 ± 0.33	10.00 ± 0.15	⋯
J0905+24	46.95 ± 0.008	46.93 ± 0.011	46.74 ± 0.008	45.49 ± 0.011	9.96 ± 0.21	9.44 ± 0.17	9.88 ± 0.15	9.94 ± 0.15	[O III]
J0257+00	46.89 ± 0.008	46.67 ± 0.013	46.22 ± 0.029	45.03 ± 0.028	10.01 ± 0.21	9.73 ± 0.16	⋯	<10.16	DPE
J2123-01	47.34 ± 0.008	47.26 ± 0.010	47.00 ± 0.009	45.62 ± 0.023	10.32 ± 0.22	9.89 ± 0.18	10.37 ± 0.21	10.05 ± 0.16	C IV
J0052+01	46.98 ± 0.008	46.86 ± 0.011	46.55 ± 0.024	45.44 ± 0.024	9.99 ± 0.21	9.71 ± 0.17	⋯	9.91 ± 0.15	⋯
J2112+00	46.81 ± 0.008	46.62 ± 0.013	46.35 ± 0.010	44.98 ± 0.028	9.96 ± 0.20	9.29 ± 0.17	9.66 ± 0.18	9.34 ± 0.15	⋯
J1027+30	46.84 ± 0.008	46.76 ± 0.013	46.61 ± 0.010	45.23 ± 0.028	9.85 ± 0.20	9.38 ± 0.17	10.11 ± 0.18	9.63 ± 0.15	⋯
J0651+38	46.65 ± 0.008	⋯	46.31 ± 0.069	44.68 ± 0.040	9.66 ± 0.20	⋯	⋯	9.15 ± 0.15	C IV
J1036+11	46.87 ± 0.008	46.97 ± 0.012	46.80 ± 0.008	45.49 ± 0.016	9.87 ± 0.20	9.53 ± 0.17	9.72 ± 0.17	9.63 ± 0.15	⋯
J0752+43	46.80 ± 0.008	46.65 ± 0.018	46.33 ± 0.012	44.90 ± 0.063	9.90 ± 0.20	9.59 ± 0.16	10.03 ± 0.16	9.64 ± 0.16	⋯
J0946+28	47.08 ± 0.008	47.02 ± 0.017	46.76 ± 0.008	45.36 ± 0.016	10.57 ± 0.27	10.14 ± 0.19	9.94 ± 0.19	9.89 ± 0.15	C IV

Note. The monochromatic continuum and broad line luminosities (erg s^{-1}), and M_{BH} values ($M_\odot$). Upper limits to the M_{BH} values are associated with double-peaked Hα emission marked as DPE in the Flags column. Extremely broad (>20,000 km s^{-1}) Fe II, highly blueshifted (>2000 km s^{-1}) C IV, and broad (>1000 km s^{-1}) [O III], are flagged Fe II, C IV, and [O III], respectively.

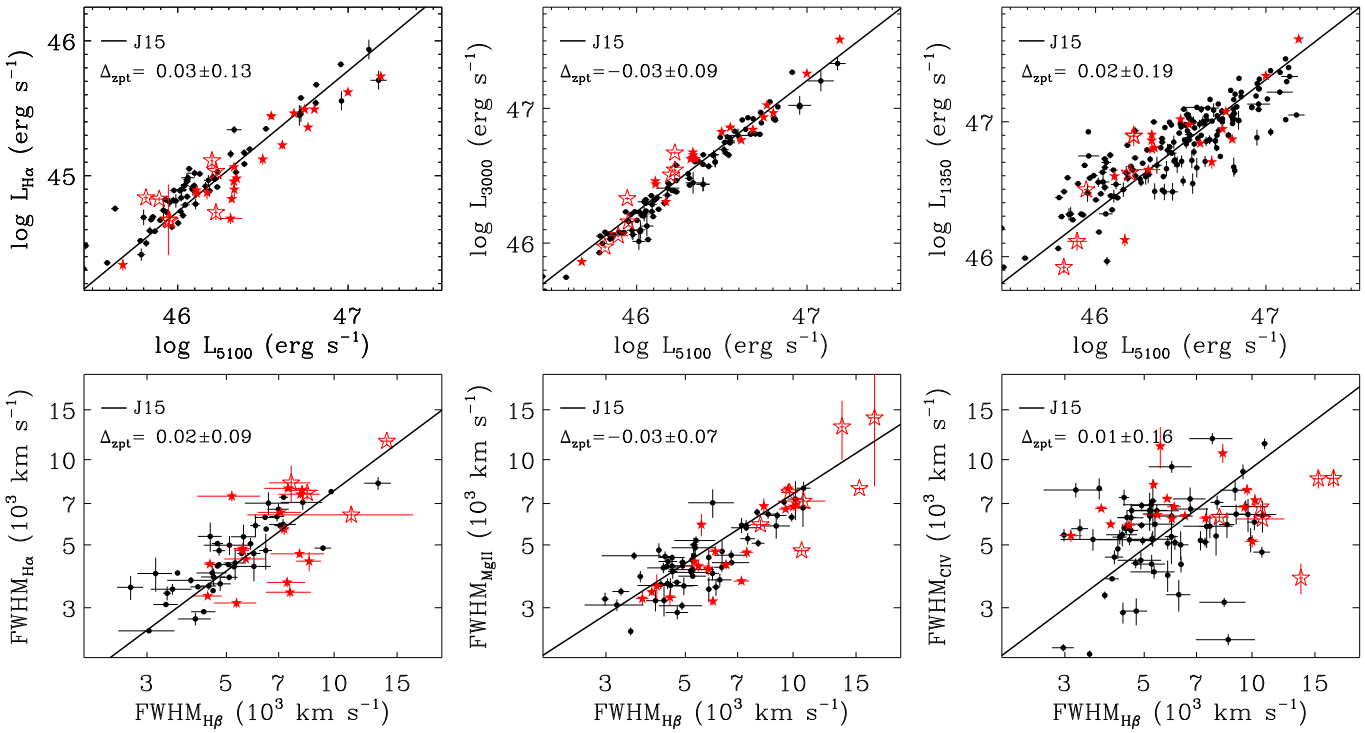

Figure 4. Continuum–line luminosity relations (top) and line width relations (bottom), for type-1 AGNs at the luminous and massive end. Among the IRTF data (red stars), those double-peaked in Hα (red open stars) are highlighted. The luminosities and line widths plotted are limited to having within 20% uncertainty, except for the double-peaked emitters. We compile the data from references spanning similarly luminous quasars as our sample (black dots, S12; J15; Shen 2016), removing FWHM$_{\rm C\,IV}$ values affected by broad absorption. The zeropoint offset of the combined data (excluding the double-peaked emitters) with respect to the J15 relation (solid lines) and intrinsic scatter are denoted as $\Delta_{\rm zpt}$. The FWHM$_{\rm H\beta}$ for the bottom right two panels are converted from FWHM$_{\rm H\alpha}$ whenever available using the J15 relation, in order to benefit from the enhanced sensitivity of the Hα line.

and Hβ line-based $M_{\rm BH}$ values, for the continuum sensitivity bins $5 < {\rm S/N_{H\beta}} < 10$ and[10] ${\rm S/N_{H\beta}} > 10$. We find $\sigma_{\rm int} = 0.21$ dex and $\sigma_{\rm int} < 0$ for the two sensitivity bins so that larger systematic uncertainties are affecting the $M_{\rm BH}$ values at lower sensitivity (e.g., Denney et al. 2009). This effect should be negligible in the Mg II, C IV, or C III] masses derived under much higher sensitivity, all at S/N > 35. We thus limit the usage of Hβ $M_{\rm BH}$ values to ${\rm S/N_{H\beta}} > 10$, and average with the Hα-based masses when used for comparison with the rest-UV $M_{\rm BH}$ values.

The estimators from J15 were calibrated to yield consistent rest-UV to rest-optical $M_{\rm BH}$ values over a wide range of luminosity and redshift, suitable for this study. We further examine where the measured continuum luminosities and broad line FWHMs of our sample with extremely large masses fall with respect to the quasars with similar luminosities. In Figures 4 and 5, we plot the continuum–line luminosity relations, FWHM relations, and the $M_{\rm BH}$ relations based on the Hα, Hβ, Mg II, and C IV lines, from this work and existing observations of similarly luminous quasars (S12, J15, Shen 2016). The offset and $\sigma_{\rm int}$ of the combined data with respect to the best-fit relations in previous works are printed on each panel. From Figure 4 we find that our objects, together with similarly luminous quasars, follow the luminosity and line width relations of J15. The data show negligible offset, and $\sigma_{\rm int}$ similar to that of the J15 relation, demonstrating that the J15 calibrations are useful even for extremely massive AGNs. We note that the extremely massive AGNs are mostly from this work and they distribute similarly in luminosity space to other luminous quasars, but have FWHM values higher than the latter. This suggests that the main factor that gives rise to EMBH estimates is their wide velocity widths.

Also, we check in Figure 5 whether the rest-UV to rest-optical $M_{\rm BH}$ values are mutually consistent at the massive end, using the J15 and S12 relations. The Hβ and Hα $M_{\rm BH}$ values of luminous, massive AGNs are consistent with each other irrespective of using the S12 or J15 estimators, albeit with a smaller intrinsic scatter for the J15 estimator due to the inclusion of the measurement uncertainties in the f-factor, $R_{\rm BLR}$–L relation, and luminosity/line width correlations. The rest-UV to Balmer $M_{\rm BH}$ values for EMBHs are mutually consistent using the J15 estimators, whereas the S12 estimators lead to systematically underestimated S12 rest-UV to J15 Balmer $M_{\rm BH}$ ratios ($\sim$0.21 and 0.40 dex underestimation in Mg II and C IV $M_{\rm BH}$ values respectively at $M_{\rm BH,H\beta} = 10^{10}\,M_\odot$, and more deviations at higher $M_{\rm BH}$). The existing estimators determined from a relatively limited dynamic range in rest-UV FWHM tend to have shallower scaling of the FWHM into the mass estimator compared to the J15, underestimating the rest-UV $M_{\rm BH}$ values at the massive end. Therefore, we keep the J15 estimator as a relatively more reliable $M_{\rm BH}$ indicator for the rest of the paper.

4.2. Mass Biasing Factors in the Spectra

4.2.1. Double-peaked Broad Emission

We find seven out of 26 broad Hα profiles classified as double-peaked emitters in Section 3 (J0203+13, J0257+00,

[10] The continuum S/N values for the denoted line in subscript letters are the median calculated over the wavelengths used to fit the line region.

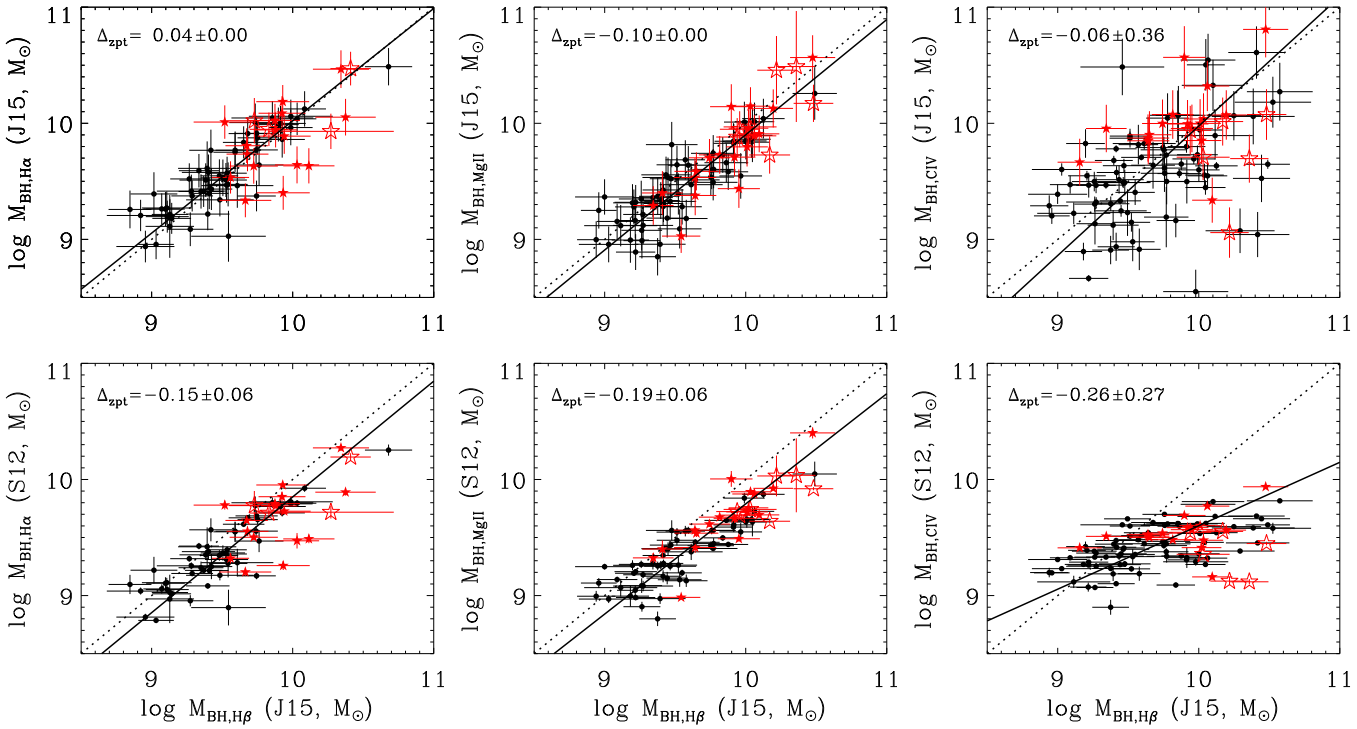

Figure 5. Massive end $M_{\rm BH}$ relations out of various lines using the J15 relation (top) and comparison of $M_{\rm BH}$ estimates between J15 and S12 (bottom), with S12 estimators corrected to have the same constant factor as the J15 ($f = 5.1$). The data, colors, and symbols follow those of Figure 4, while the $M_{\rm BH}$ values plotted are limited to having within 0.3 dex uncertainty except for the double-peaked emitters. The zeropoint offset of the combined data with respect to a one-to-one relation and intrinsic scatter (fixed to zero when negative) are denoted as $\Delta_{\rm zpt}$. The linear fit to the data and a one-to-one relation are shown in solid and dotted lines respectively. The double-peaked emitters are excluded for the $\Delta_{\rm zpt}$ calculation and the linear fit. The $M_{\rm BH,H\beta}$ for the center and right panels are converted from $\rm FWHM_{H\alpha}$ whenever available using the J15 relation, in order to benefit from the enhanced sensitivity of the Hα line.

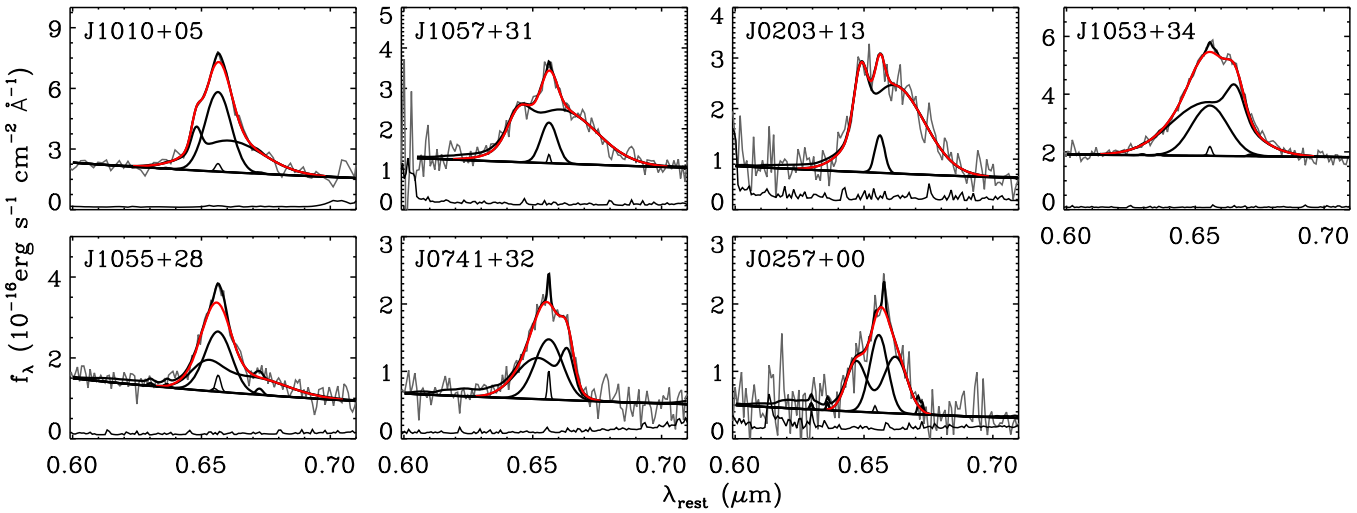

Figure 6. Hα profiles of double-peaked emitters identified using triple broad Gaussian fitting. The combined blue- and redshifted double-peaked broad emission and the central single broad emission components are separately plotted (thick black), as well as the total broad (red) and the narrow emission (thin black). The noise spectrum is shown below the object spectrum.

J0741+32, J1010+05, J1053+34, J1055+28, J1057+31), best fit as triple Gaussians with clear blue- and redshifted components comparable in strength or dominating over the central broad component. In Figure 6, we plot the Hα fit and the noise spectrum of the double-peaked emitters, and find that the double-peaked features are stronger than the noise levels. We follow Baskin & Laor (2005) to place these objects along various parameters describing their profile: the shape, (FW1/4M + FW3/4M)/(2FWHM); the asymmetry, $(\lambda_{3/4}-\lambda_{1/4})$/FWHM; and the shift, $(\lambda_{3/4}-\lambda_{4/4})$/FWHM, where FWN/4M and $\lambda_{N/4}$ (N = 1–4) are the width and centroid of the Nth-quarter maximum of the line. The shape parameter for the seven double-peaked objects ranges within 0.89–1.16 (1.03 on average), shifted to the distribution of 1.02–1.37 (1.16 on average) for the non-double-peaked objects and lying on the smaller end of the Hβ distribution from Baskin & Laor (2005).

The distribution of asymmetry and shift parameters are indistinguishable between the double-peaked and ordinary profiles. Overall, our selected double-peaked profiles are systematically different to ordinary profiles as being wider toward the peak or the wings. However, we still caution against directly comparing our double-peaked profiles to those in the literature, as some examples (J1010+05, J1055+28) look marginal in appearance.

From Figure 4, we find the double-peaked emitters are slightly above the J15 L_{5100}–$L_{\rm H\alpha}$ relation by 0.068 dex on average, though within $\sigma_{\rm int} = 0.095$ dex from the J15 relation. Also, the double-peaked emitters lie below the $\rm FWHM_{H\beta}$–$\rm FWHM_{C\,IV}$ relation by −0.24 dex on average, slightly larger than $\sigma_{\rm int} = 0.21$ dex from the J15 relation. We further estimate the differences in the Hα and C IV $M_{\rm BH}$ estimates for the double-peaked emitters, to find $\log M_{\rm BH,H\alpha}/M_{\rm BH,C\,IV} = -0.01$–1.15 (0.45 on average). The C IV spectra of double-peaked Hα emitters appear to show weaker double-peaks (e.g., Eracleous et al. 2004), which is consistent with the larger $\rm FWHM_{H\alpha}$ to $\rm FWHM_{C\,IV}$ ratios for our double-peaked emitters, 0.01–0.44 dex (0.16 dex on average).

We independently check whether using the line widths for double-peaked Hα emitters lead to overestimated $M_{\rm BH}$ values (e.g,. Wu & Liu 2004; Zhang et al. 2007), from the stellar velocity dispersion (σ_*) and $\rm FWHM_{H\alpha}$ measurements of 10 double-peaked emitters from Lewis & Eracleous (2006), where we find nine objects having both σ_* and $\rm FWHM_{H\alpha}$ compiled from the literature (Eracleous & Halpern 1993, 1994; Barth et al. 2002; Sergeev et al. 2002; Nelson et al. 2004; Lewis & Eracleous 2006; Lewis et al. 2010). Applying the $M_{\rm BH}$–σ_* relations from Kormendy & Ho (2013) and McConnell & Ma (2013) gives a range of $M_{\rm BH}(\sigma_*)$ values, considering that the slope of the relation is different between the references. Meanwhile, we converted the bolometric luminosities in Lewis & Eracleous (2006) to L_{5100} using the bolometric correction 10.33 from Richards et al. (2006a), to estimate the $M_{\rm BH,H\alpha}$ using the J15 estimator. We use only objects with $L_{5100} > 10^{41.5}$ erg s^{-1} where the mass calibration is defined, yielding six $M_{\rm BH}$ estimates. To minimize the time-dependent changes in $\rm FWHM_{H\alpha}$, we use the averaged value through monitored observations available for four objects. Assuming that the double-peaked emitters are lying on the $M_{\rm BH}$–σ_* relation, we find the $M_{\rm BH,H\alpha}$ values are larger than the $M_{\rm BH}(\sigma_*)$ values by 0.32–1.14 dex (0.85 dex on average), and 0.32–2.06 dex (1.01 dex on average), out of the Kormendy & Ho (2013) and McConnell & Ma (2013) relations respectively. This is in agreement with the Zhang et al. (2007) result.

We make a cautionary note that the $M_{\rm BH}$ estimates thought to be less affected by the double-peaked features involve large intrinsic scatter (∼0.4 dex for the $M_{\rm BH,C\,IV}$ from J15, ∼0.3–0.4 dex for the $M_{\rm BH}(\sigma_*)$ from Kormendy & Ho 2013; McConnell & Ma 2013), and the bolometric luminosities in Lewis & Eracleous (2006) suffer from incomplete wavelength coverage. Still, the overestimation in $M_{\rm BH}$, comparable to or even more sizable than the uncertainties, suggests that the $M_{\rm BH}$ values of double-peaked emitters using the full broad Balmer emission profile are possibly overestimated. We find that four objects out of the seven double-peaked Hα emitters with Hβ S/N > 5 have relatively broad $\rm FWHM_{H\beta}$ values of 7600–14,000 km s^{-1} (10,300 km s^{-1}on average) compared to 4430–8500 km s^{-1} (6580 km s^{-1}on average) for the rest of the sample. Our Hβ observations have poorer sensitivities than the Hα to identify double-peaked emission, but the FWHMs are consistent with the expected broadening of the line profile from a rotating accretion disk.

4.2.2. Extremely Wide Fe II Solution Near Mg II

Next, we investigate the effect of Fe II subtraction on the systematic uncertainty of the $M_{\rm BH}$ estimates. Whereas most of the Hβ spectral fits in Section 3 yielded a least-squares solution for the Fe II complex,[11] four out of 25 Mg II spectra (J0146-10, J0203+13, J1053+34, J1057+31) did not converge until the $\rm FWHM_{Fe\,II}$ reached its maximum limit of 20,000 km s^{-1}, with the first three classified as double-peaked emitters from the Hα spectra. We note that the automated fitting of SDSS spectra from Shen et al. (2011) also identifies extremely broad Fe II solutions within our sample (J1010+05, J1053+34, J1057+31, J1522+52), with the first three double-peaked in our Hα. To improve the Mg II fit of these sources we attempted to include a Balmer continuum emission component that is usually degenerate with the power-law continuum and the Fe II complex (e.g., Maoz et al. 1993; Wang et al. 2009), following the functional form and parameter boundaries of S12. Fitting both the power-law and Balmer continuua does not reduce the extremely wide Fe II widths to convergence for all four of our sources, however, such that either the standard Fe II template does not fit these quasar spectra, or the broad Gaussian model is insufficient to model these Mg II profiles. In any case, the $M_{\rm BH}$ measurements associated with extremely broad Fe II solutions require careful interpretation as they correlate with sources showing double-peaked Hα emission.

4.2.3. Blueshifted C IV

Third, though it is typical to find C IV emission in quasar spectra blueshifted relative to the rest-optical or Mg II redshifts by ∼1000 km s^{-1} (e.g., Richards et al. 2002; Shen et al. 2008, 2011), we find stronger blueshifts in our sample. For comparison, the mean and rms scatter of the C IV to Mg II blueshift from SDSS DR7 quasars at $1.6 < z < 2.0$ with S/N > 20 in both Mg II and C IV is 844 ± 916 km s^{-1} (Shen et al. 2011). Seven out of 12 (58%) of the objects in our sample that are not double-peaked emitters and have fits to both Mg II and C IV show C IV to Mg II blueshifts exceeding the 1-σ limits of the SDSS sample distribution (>1760 km s^{-1}). This fraction for the SDSS comparison sample is only 107/728 (15%). In Figure 7 top panels, we show the best-fit broad line models of the five objects in our sample with the largest C IV to Balmer blueshifts. The Hβ, Hα, Mg II, and C IV fits are plotted on top of each other, normalized in height and shown relative to the Hα redshift. Interestingly, the spectra showing the largest C IV blueshifts (∼5000–6000 km s^{-1}, J0946+28, J1522+52) have sequentially decreasing, but measurable, blueshifts toward Mg II and Hβ. The blueshifted C IV profiles often appear asymmetric, skewed toward extreme blueshifts (∼10,000 km s^{-1}), and the asymmetry continues to appear in some of the Mg II and Balmer lines.

We follow Baskin & Laor (2005) to place these blueshifted C IV quasars along the shape, asymmetry, and shift parameters describing their profiles. The shape parameter ranges within 1.05–1.46 (1.16 on average) for the 11 objects with C IV blueshift smaller than 2000 km s^{-1}, and 1.05–1.49 (1.16 on

[11] The exceptions are the Fe II fitted with the narrowest widths (900 km s^{-1} from the template, J0748+22, J0905+24), but they are acceptable considering that the Fe II of these objects are too weak to be well constrained.

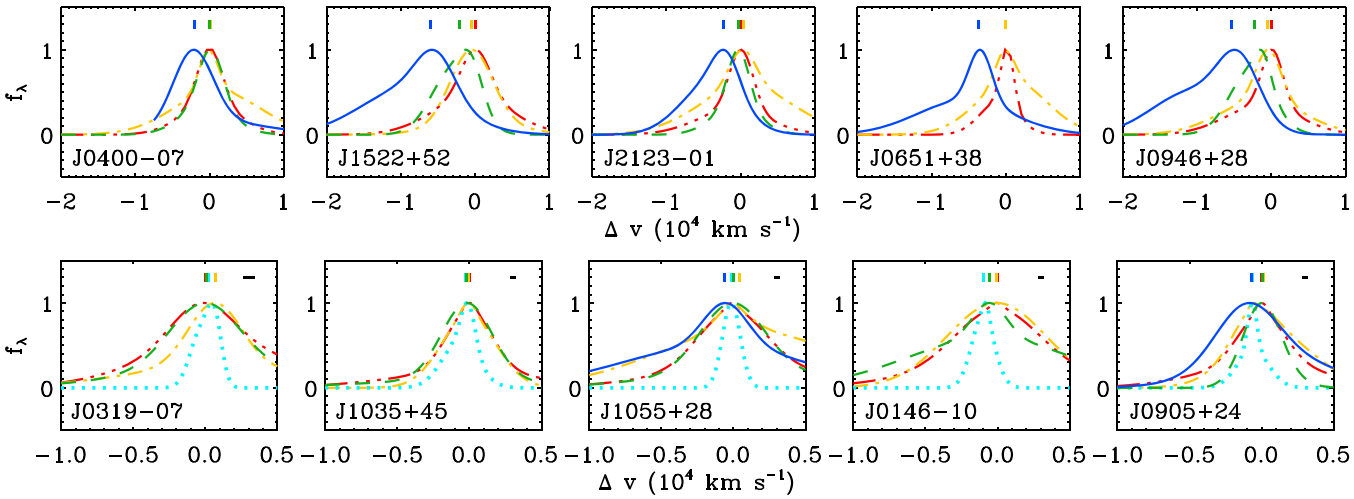

Figure 7. Top: normalized, broad line model profiles of Hα (red triple dotted–dashed), Hβ (yellow dotted–dashed), Mg II (green dashed), and C IV (blue solid) for five objects with the most highly blueshifted C IV emission, along the line-of-sight velocity measured with respect to the broad Hα redshift. Negative velocities indicate blueshift, and the centers of each broad line model are marked. The colors for the lines follow those of Figure 3. Bottom: normalized, [O III], Hα, Hβ, Mg II, and C IV model profiles for five objects with [O III] FWHM > 1000 km s^{-1} at peak S/N > 5, along the line-of-sight velocity measured with respect to the broad Hα redshift. The [O III] are colored cyan and dotted, while other lines are visualized as the top panels. The instrumental resolution elements are denoted as black horizontal lines on the top right of each panel.

average) for the five objects with C IV blueshift larger than 2000 km s^{-1}. The indistinguishable distribution of the shape parameter indicates that the FWHM is a good indicator of the overall line shape, irrespective of the C IV blueshift (but see also Coatman et al. 2016 for the changing ratios between FWHM and σ along the C IV blueshift). On the other hand, the asymmetry parameter is preferentially distributed toward excess blue wings at highly blueshifted C IV, −0.10–0.12 (0.02 on average) and −0.04–0.35 (0.20 on average) for objects with C IV blueshift smaller and larger than 2000 km s^{-1}, respectively. Furthermore, the shift parameter goes more negative at highly blueshifted C IV, −0.32 to −0.10 (−0.21 on average) and −0.67 to −0.31 (−0.41 on average) for objects with C IV blueshift smaller and larger than 2000 km s^{-1}, respectively. Having seen the asymmetric, blueshifted nature of the C IV profiles that are suggestive of obscuration or outflows in Baskin & Laor (2005), we investigate whether the C IV $M_{\rm BH}$ shows any systematic offset to the Balmer $M_{\rm BH}$ at higher blueshift. Indeed, we find that the C IV $M_{\rm BH}$ values of the five objects showing C IV to Hα blueshifts >2000 km s^{-1} (J0400−07, J0651+38, J0946+28, J1522+52, J2123−01), are positively offset with respect to the Hα $M_{\rm BH}$ values by 0.26–0.68 dex (0.41 dex on average).

4.2.4. Ionized Outflows

Finally, we find a handful of blueshifted narrow [O III]λ5007 emissions that are wider than the typical narrow lines. Nine out of the 21 objects with an Hβ region fit have unambiguous [O III] profiles and peak S/N > 5, where five of them meet FWHM$_{\rm [O\,III]} > 1000$ km s^{-1} (J0146−10, J0319−07, J0905+24, J1035+45, J1055+28). In Figure 7, bottom panels, we plot the best-fit model for the [O III] and broad emission lines of these five objects. We find that the [O III] profiles are typically blueshifted by a few hundred km s^{-1} relative to the broad Balmer redshift, and the FWHMs reach up to 1600–1900 km s^{-1} (J0146−10, J0319−07, J1035+45). These [O III] line widths are too broad to be explained by even the most massive galaxy's gravitational potential (FWHM ~ 1000 km s^{-1}), and are broad relative to quasars at comparable luminosity or redshift (e.g., Netzer et al. 2004; Brusa et al. 2015; Shen 2016). Previous work on broad [O III] emission in quasars shows that the width correlates with its blueshift, indicative of strong outflows (e.g., Liu et al. 2014; Zakamska & Greene 2014). We therefore investigate the effect of fixing the width of narrow lines around the Hα for the objects with [O III] profiles broader than FWHM $= 1000$ km s^{-1}, bearing in mind they were fixed to 1000 km s^{-1} in Section 3. We fit the Hα region by first fixing the narrow line FWHM to that of the [O III] assuming all the narrow lines are fully broadened as the [O III], and to 400 km s^{-1} (the mean FWHM$_{\rm H\alpha}$ of local quasars used in Section 3) assuming they are completely absent of outflows, respectively, where the FWHM$_{\rm H\beta}$ of quasars with broad [O III] for example, seem to lie in between (Zakamska & Greene 2014). When the narrow line widths are fixed to that of the [O III] instead of 1000 km s^{-1} the Hα $M_{\rm BH}$ values vary by −0.01 to 0.12 dex (0.03 dex on average), and by −0.07 to 0.02 dex (−0.02 dex on average) when fixed to 400 km s^{-1}. The limited differences in the $M_{\rm BH}$ values indicate that the effect of narrow line outflows, whether or not present at the Hα region, is negligible in determining the broad line widths of extremely massive quasars.

4.2.5. Summary of Biases from Spectra

In Figure 8, we compare the rest-optical and rest-UV $M_{\rm BH}$ values determined from Section 3, marking the sources with unusual spectral features addressed here. We calculate how much the $\sigma_{\rm int}$ values between the rest-optical and rest-UV $M_{\rm BH}$ values decrease as we remove each class of unusual spectra. There is a general agreement between the Balmer and rest-UV line-based masses up to $\sim 10^{10}\,M_\odot$ with a much smaller scatter between the Balmer and Mg II-based masses ($\sigma_{\rm int} < 0$) than between the Balmer and C IV-based masses ($\sigma_{\rm int} = 0.33$ dex). This is in accord with earlier results from relatively less massive regimes (e.g., Shen et al. 2008; J15). The $\sigma_{\rm int}$ between the Balmer and C IV $M_{\rm BH}$ values drops from $\sigma_{\rm int} = 0.33$ dex to 0.23 dex when the double-peaked emitters are excluded, and down to $\sigma_{\rm int} = 0.16$ dex when objects with C IV

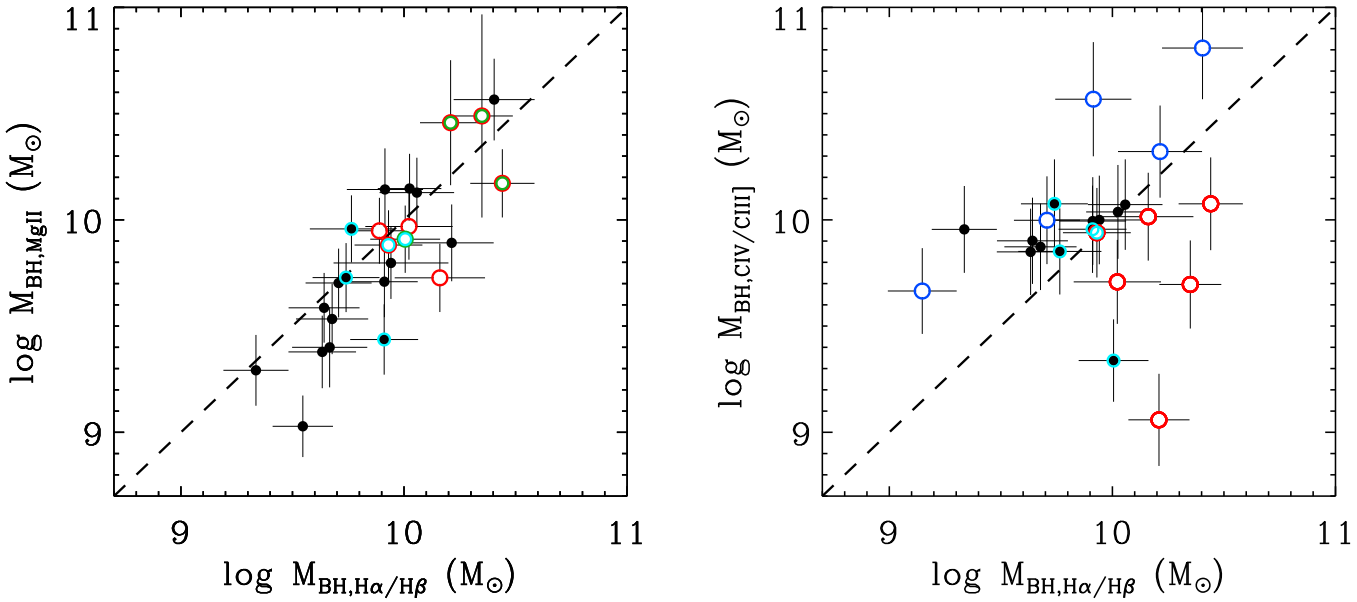

Figure 8. Comparison of rest-optical and rest-UV $M_{\rm BH}$ values at the massive end. The Hα and Hβ $M_{\rm BH}$ values are averaged when S/N$_{\rm H\beta}$ > 10; Hα values are used otherwise. The C III] $M_{\rm BH}$ values are plotted when C IV is absent; C IV values are used otherwise. Sources with double-peaked Hα emission (red), extremely broad Fe II around Mg II (green), and broad C IV blueshifted by more than 2000 km s^{-1} relative to broad Hα (blue), have significant effect on the mass estimates and are marked with open circles. [O III] lines with FWHM > 1000 km s^{-1} (cyan) are negligibly ($\lesssim$0.1 dex) affecting the mass estimates and are marked with filled circles.

blueshifts >2000 km s^{-1} are further omitted. The number of $M_{\rm BH} > 10^{10}\,M_\odot$ AGNs drops from 10, 7, 8 based on Balmer-, Mg II-, and C IV-based measurements, to 5, 4, 5 after removing the double-peaked Hα emitters, extremely broad Fe II around the Mg II, and highly blueshifted C IV sources, respectively. This suggests that $M_{\rm BH}$ values $\gtrsim 10^{10}\,M_\odot$ from any line should be carefully inspected for unusual features appearing in or on top of the broad lines.

4.3. Mass Biasing Factors in Using the Estimator

4.3.1. f-factor

When bringing the spectral measurements into the single-epoch $M_{\rm BH}$ estimators, we consider the variations in the constant of the $M_{\rm BH}$ equation for AGNs (f-factor) that gives an overall normalization but is inaccurate for individual mass measurements. Because this constant is obtained from normalizing the zeropoint of the $M_{\rm BH}$–σ_* relation, it has a systematic uncertainty of 0.3–0.4 dex (e.g., Kormendy & Ho 2013; McConnell & Ma 2013). Using a constant f-factor as a representative value could overestimate the $M_{\rm BH}$ values for objects with anisotropic radiation or velocity dispersion (e.g., Peterson et al. 2004), when the line-of-sight values of these quantities are observed to be larger than geometrically averaged. To check whether the $M_{\rm BH} \sim 10^{10}\,M_\odot$ estimates can be explained by large line-of-sight spectral quantities of less massive BHs, we compared the average and rms scatter of the L_{5100} and FWHM$_{\rm H\alpha}$ from our sample excluding the double-peaked emitters, divided by groups with $M_{\rm BH,H\alpha}$ values smaller and larger than the median, $10^{9.9}\,M_\odot$. The averaged luminosities are $\log(L_{5100}/{\rm erg\ s^{-1}}) = 46.38 \pm 0.32$ and 46.55 ± 0.38 respectively, where the average difference in the luminosities correspond to a 0.08 dex difference in $M_{\rm BH}$, much smaller than the difference in the average $M_{\rm BH}$ between the two groups, 0.52 dex. This suggests that EMBH masses are not caused by the continuum luminosities that are boosted to unusually large values due to mechanisms like anisotropic accretion or gravitational lensing. Meanwhile, the averaged line widths are FWHM$_{\rm H\alpha} = 3920 \pm 960$ and 6210 ± 1390 km s^{-1}, respectively, showing that $\gtrsim 10^{10}\,M_\odot$ estimates are influenced by large FWHM values that could be caused by anisotropic velocity field. However, this does not rule out the case where the line widths of extremely massive AGNs are intrinsically wide due to the stronger gravitational potential from the BH.

There are issues of whether the f-factor is systematically different (up to ~0.3 dex) between AGN subsamples grouped by host galaxy and BH properties, and also the limited statistical significance and dynamic range in the constraints to the f-factor (e.g., McConnell & Ma 2013; Woo et al. 2013; Ho & Kim 2014). The local $M_{\rm BH}$–σ_* relation for AGNs at least, which covers up to $\sim 10^9\,M_\odot$ BHs, does not differ in $\sigma_{\rm int}$ with respect to inactive galaxies (e.g., Woo et al. 2013). The spatially resolved direct dynamical $M_{\rm BH}$ measurement for inactive galaxies is thought to be much more accurate than the $M_{\rm BH}$ estimate for AGNs using a constant f-factor, and the $\sigma_{\rm int}$ for AGNs is expected to be significantly larger than that for inactive galaxies if there was a large intrinsic dispersion in the f-factor. The indistinguishable $\sigma_{\rm int}$ values for AGNs support that the $M_{\rm BH}$–σ_* relation itself is intrinsically scattered rather than the f-factor, which hints that the EMBHs in luminous quasars are intrinsically massive rather than positively biased in mass. Alternatively, the widespread distribution of FWHM$_{\rm H\beta}$ to Fe II strengths for type-1 quasars are interpreted as the geometric orientation playing a significant role in the observed dispersion of the FWHM$_{\rm H\beta}$ values (e.g., Shen & Ho 2014). Still, the luminous, intermediate-redshift type-1 quasar samples of S12 and Shen (2016) reaching up to EMBH masses show broader FWHM$_{\rm H\beta}$ values than the less luminous, local quasars in Shen et al. (2011), which they claim as due to intrinsically broader line width or more massive BHs for the S12 and Shen (2016) samples. Further study of the $M_{\rm BH}$–σ_* relation at the

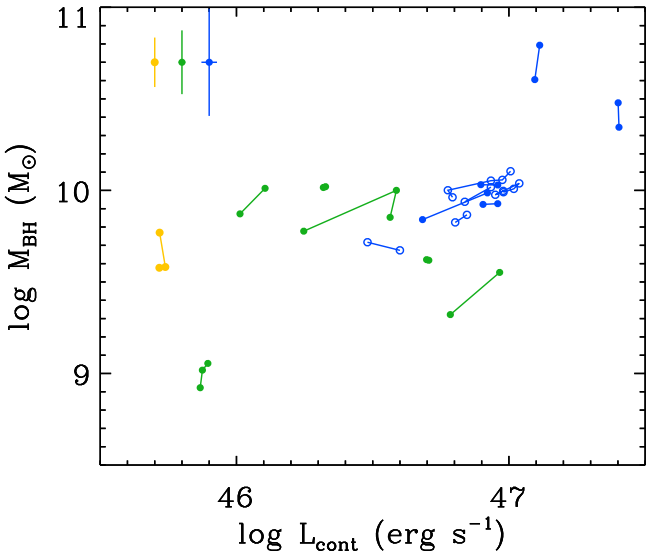

Figure 9. Single-epoch $M_{\rm BH}$ values for objects with multiple epoch SDSS spectra, plotted against the continuum luminosity $L_{\rm cont}$ (L_{5100} for Hβ, L_{3000} for Mg II, L_{1350}/L_{1450} for C IV). The colors for the Hβ, Mg II, and C IV line-based values follow those in Figure 2. $M_{\rm BH}$ values from the same object are connected, and we mark the C IV masses with open and filled circles to differentiate the objects. The mean $M_{\rm BH}$ uncertainty from each line-based estimator is shown in the upper left.

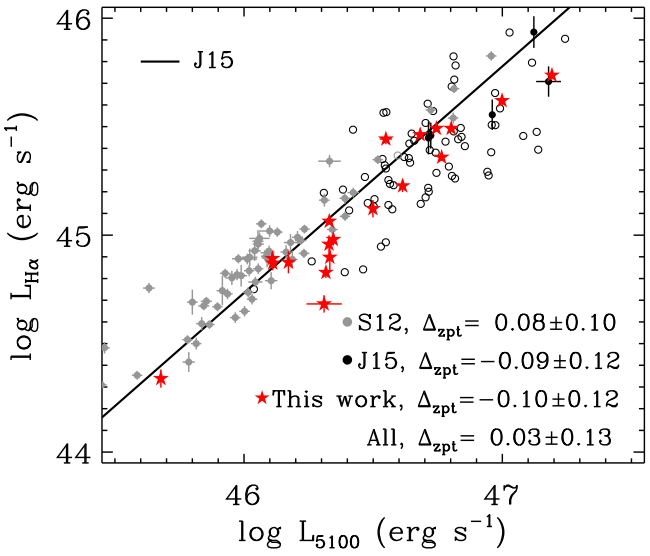

Figure 10. L_{5100}–$L_{\rm H\alpha}$ relation revisited at the luminous end. We plot data points from S12, J15, and this work (removing the double-peaked emitters) in gray, black, and red, and labeled S12, J15, and this work respectively. The luminosities are limited to having within 20% uncertainty (filled symbols) and above 20% uncertainty (open symbols). The J15 relation is overplotted as a black line, and the offset and 1-σ scatter of the data points (within 20% uncertainty) to the relation are listed for each sample.

massive end, especially for active galaxies, and detailed modeling of the velocity structure of the BLR (e.g., Brewer et al. 2011; Pancoast et al. 2014) are crucially required to better understand whether EMBH masses are either a geometric selection or intrinsic property.

4.3.2. Variability

Second, the $M_{\rm BH}$ estimators could suffer from variability such that the single-epoch measurements may not be representative values. Also, the time lag of the continuum to reach the BLR hinders obtaining coherent continuum luminosity and broad emission width from a given epoch. To probe the extent of continuum variability, we compiled the Catalina Real-time Transient Survey (Drake et al. 2009) optical light curves of our sample spanning eight years on average. We calculated the variability amplitude $\sigma_{\rm var}$ where $\sigma^2_{\rm var} = \Sigma_{i=1}^{N}\{(m_i - \bar{m})^2 - \Delta m_i^2)\}/(N-1)$ for the mean magnitude $\bar{m}$ and N magnitude and error measurements (m_i, Δm_i), and find the $\sigma_{\rm var}$ value to range within 0.27 (median of 0.08) mag. This level of intrinsic variation in the optical continuua is small, and even the object with the largest magnitude variation has a corresponding luminosity variation of 0.11 dex, or an $M_{\rm BH}$ variation of 0.05 dex. To further investigate the emission line variability, we plot in Figure 9 the single-epoch $M_{\rm BH}$ values from multi-epoch SDSS spectroscopy with connected symbols. We do not perform secondary flux calibration to the spectra (e.g., Section 2.2) so that the variations in the spectral continuum includes the contribution from imperfect spectral flux calibration. Excluding the single object without a converging Fe II solution around the Mg II region (J0146 −10), we have 1, 6, 10 objects with multi-epoch (2–5 visits) $M_{\rm BH}$ measurements in Hβ, Mg II, and C IV, respectively. We find that the $M_{\rm BH}$ values fall within their errors throughout the sparsely covered epochs. Overall, the minor level and effect of variability on the single-epoch $M_{\rm BH}$ estimates for extremely massive AGNs, is consistent with the trends at lower masses (e.g., Park et al. 2012; Jun & Im 2013).

4.3.3. Overestimated Ionizing Continuum

Third, we investigate cases where the observed AGN luminosities and broad line widths may not be applied to the standard $M_{\rm BH}$ equation. J15 report that the rest-optical continuum luminosity of extremely luminous AGNs ($L_{5100} \sim 10^{47}$ erg s^{-1}) marginally overestimates the ionizing luminosity as traced by the Hα line luminosity, perhaps hinting that the accretion disk of extremely massive and low-spin BHs does not produce sufficient ionizing radiation (e.g., Laor & Davis 2011; Wang et al. 2014). In Figure 10 we examine the luminous end L_{5100}–$L_{\rm H\alpha}$ relation, including our IRTF data points. We find that the IRTF data are mildly below the J15 relation, but do not show a systematic trend with L_{5100}. Further imposing a 20% uncertainty limit to the combined data, most of the negatively offset outliers from J15 are removed so that the downward trend of the relation at the highest luminosities is less likely with higher-sensitivity data. We also find that the IRTF data improve the completeness of the relation at $L_{5100} \sim 10^{46}$ erg s^{-1}, filling the weaker emission line AGNs less covered by S12. The combined, sensitivity cut data in Figure 10 show a 0.03 $\pm$ 0.13 dex offset and scatter to the J15 relation, supporting that the slope of the L_{5100}–$L_{\rm H\alpha}$ relation stays universal across $L_{5100} \sim 10^{42-47}$ erg s^{-1} and that cold accretion disks in low-spin EMBHs, if any, have a minor effect ($\lesssim$0.1 dex) in positively biasing the $M_{\rm BH}$ estimates derived using L_{5100} instead of $L_{\rm H\alpha}$.

4.3.4. FWHM versus σ

Finally, we further look into the possible bias of using the broad line FWHM rather than the σ. Although the FWHM is technically simple to measure and is less affected than σ by

Table 4
Double-peaked Emitter Fraction along FWHM and L_{5100}

log L_{5100}	FWHM$_{H\alpha}$ <2000	2000–4000	4000–6000	6000–8000	>8000
44.6–44.9	0.00–0.02	0.02–0.12	0.14–0.36	0.22–0.59	0.78–0.83
44.3–44.6	0.00–0.00	0.01–0.13	0.12–0.31	0.14–0.52	0.23–0.48
44.0–44.3	0.00–0.00	0.02–0.12	0.05–0.23	0.17–0.38	0.27–0.44

Note. The fraction of $z < 0.37$, S/N > 10, type-1 quasars in Shen et al. (2011) that are classified as highly double-peaked, and highly/weakly double-peaked are shown in ranged values. The L_{5100} and FWHM$_{H\alpha}$ are in units of erg s^{-1} and km s^{-1}, respectively.

weakly constrained wings at poor sensitivity, it could be relatively inaccurate when the line profiles are far from a universal shape (e.g., Peterson et al. 2004; Collin et al. 2006). The M_{BH} estimators in J15 assume a constant FWHM $= 2\sigma$ condition for the broad Hβ line widths, but any deviation from this constant could bias the M_{BH} estimates derived using FWHM. We checked whether our sample exhibits this constant relation between the Hα FWHM and σ values determined from Section 3. We find that the mean and rms scatter of the FWHM to σ ratios of the 21 objects without double-peaked emitters are mildly smaller than 2 (FWHM$/\sigma = 1.5 \pm 0.3$) and thus the EMBH masses are less likely to be spuriously overestimated by using FWHM instead of σ. In fact, when assuming that the $M_{BH,H\beta}$ scales proportional to $\sigma^2_{H\beta}$ and FWHM$_{H\alpha} = 2\,\sigma_{H\alpha}$, the $\sigma_{H\alpha}$-based $M_{BH,H\alpha}$ values from Equations (1) and (2) would change from the FWHM-based values by −0.09–0.55 dex (0.30 dex on average), nearly doubling the non-double-peaked, $M_{BH,H\alpha} > 10^{10}\,M_\odot$ objects from 7 to 13. Interestingly, the FWHM to σ ratios for the double-peaked emitters are somewhat larger than the rest of the sample (average and rms scatter of 2.2 ± 0.4) so that they will be better noticed by extremely wide FWHMs rather than σ values.

5. Discussion

5.1. M_{BH} Bias Due to Double-peaked Lines

In the previous section, we considered cases where the M_{BH} estimates of AGNs, including those in the EMBH regime, could be systematically biased. Here, we investigate whether the two largest factors associated with possibly overestimated M_{BH} values, double-peaked broad emission, and blueshifted C IV, are preferentially selected toward EMBH masses, or if they are conditionally appearing in general type-1 quasar spectra. We begin by comparing the double-peaked emitter fraction to those from the literature with larger samples at $z \lesssim 0.4$. Our double-peaked emitter fraction, (5–7)/26 (19%–27%),[12] is comparable to or higher than 20% among 106 radio-loud AGNs (Eracleous & Halpern 2003), and much higher than 3% out of 3216 optically selected quasars (Strateva et al. 2003), although the fraction is dependent on the parameter space where the double-peaked emitters are examined and the definition of being double-peaked. The double-peaked emitters show broader FWHM$_{H\alpha}$ than typical AGNs, distributed mostly above 5000 km s^{-1} and comparable in number to the non-double-peaked at above 8000 km s^{-1} (Eracleous & Halpern 2003; Strateva et al. 2003). Our study is in agreement with the expectation that 5/7 double-peaked emitters reach FWHM$_{H\alpha} > 8000$ km s^{-1} while none of the rest of the objects' widths exceed this limit.

We further examine whether the double-peaked emitters generally have extremely wide FWHMs by using the visually classified double-peaked emitters in Shen et al. (2011). We cut their sample to $z < 0.37$, S/N > 10 to probe the double-peaked Hα fraction, with their special interest flag selected as either highly double-peaked only, or highly/weakly double-peaked. Table 4 shows double-peaked emitter fractions per luminosity and FWHM bin, where the average uncertainties of the fractions are 0.34 and 0.21 times the fraction, for highly double-peaked cases and highly/weakly double-peaked cases respectively. We find that there is a mild increase of the double-peaked emitter fraction at higher L_{5100} with a fixed FWHM, but the fraction increases more significantly with FWHM at a fixed L_{5100}. This suggests that extremely wide FWHMs are likely to be associated with double-peaked emitters, regardless of the M_{BH}. We note that some double-peaked emitters could be missed for a variety of reasons. For instance, the line-emitting accretion disk model (e.g., Chen & Halpern 1989) predicts that the double-peaks may not be detached at small inclination angles ($i \lesssim 10°$) and look like ordinary broad emission. This adds the ambiguity of whether the observed broad lines in type-1 AGNs are coming from random motions of broad line clouds or Keplerian rotation of a disk, and they may be separated by velocity-resolved reverberation measurements of the line-emitting region size (e.g., Dietrich et al. 1998; O'Brien et al. 1998).

Interestingly, the Mg II spectra of double-peaked Hα emitters also often exhibit double peaks that are weaker or appear blended (e.g., Eracleous & Halpern 2003; Eracleous et al. 2004, 2015). These features in our sample are weak (J0203+13) or hard to tell (J0257+00, J0741+32, J1010+05, J1053+34, J1055+28, J1057+31), somewhat consistent with the literature, and explains why our double-peaked Hα emitters were not flagged out by rest-UV spectra in Section 2.1. This indicates the likelihood that double-peaked emission is ambiguously mixed on top of the broad Mg II line, placing negative implications on the reliability of M_{BH} measurement from the Mg II line alone at wide FWHM values. Furthermore, we reviewed that extremely wide Fe II around Mg II could be associated with overestimated Mg II width solutions (Section 4.2.2). The lower limit of FWHM$_{Mg\,II}$ when this occurred in our sample is 6800 km s^{-1} from our analysis, and 6900 km s^{-1} from the automated spectral fitting of Shen et al. (2011). Caveats of using the broadest FWHM$_{Mg\,II}$ for M_{BH} measurements are in line with existing studies where the rotational broadening is able to fully explain the observed FWHMs only up to 4000–6500 km s^{-1} in typical BLRs (e.g., Kollatschny & Zetzl 2013; Marziani et al. 2013). We also note

[12] We consider J1010+05 and J1055+28 marginally double-peaked and provide the range of fractions depending on the inclusion of these objects.

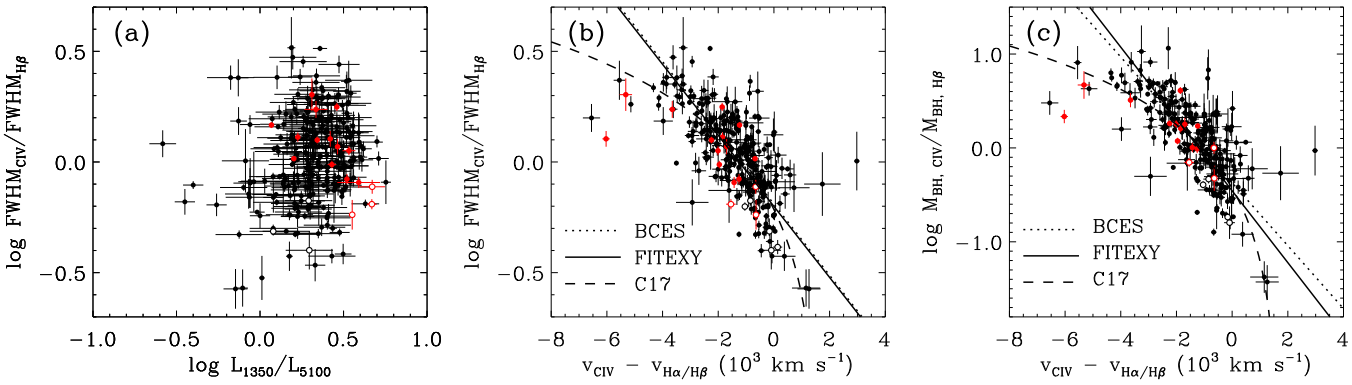

Figure 11. Ratio between C IV and Balmer broad line FWHMs plotted against rest-frame 1350–5100 Å continuum luminosity ratio (left) and Balmer to C IV broad line shift (center), and the M_{BH} ratio against C IV blueshift (right). Negative velocities indicate blueshift. The Balmer to C IV shifts are averaged when both the Hα and Hβ lines are observed, and the FWHM$_{H\beta}$ is converted from FWHM$_{H\alpha}$ whenever available using the J15 relation, in order to benefit from the enhanced sensitivity of the Hα line. We plot the data points from the literature (Netzer et al. 2007; Shang et al. 2007; Dietrich et al. 2009; Assef et al. 2011; Ho et al. 2012; S12; Bentz et al. 2013; Park et al. 2013; J15; Mejía-Restrepo et al. 2016; C17 and references within) converted to our adopted cosmology in black, and from this work in red. We limit the line width ratios and luminosity ratios to sources with <0.15 dex uncertainties, and the line shifts to sources with <1000 km s^{-1} uncertainties. Objects with broad absorption lines near the C IV line are rejected, while objects with FWHM$_{H\alpha}$ > 8000 km s^{-1} among the literature or those classified as double-peaked emitters from this work are shown as open circles. The two objects in Shang et al. (2007) that overlap with Park et al. (2013) are removed, while the L_{1350} and FWHM$_{C\,IV}$ from Netzer et al. (2007) are updated to the values from Shen et al. (2011). On panel (b) the FITEXY and BCES fit to the filled data are shown in solid and dotted lines, respectively, while the C17 relation (corrected as $M_{BH} \propto$ FWHM^2 for panel (c)) is overplotted (dashed line).

that the FWHMs of the highly blueshifted (>2000 km s^{-1} relative to Hα, Section 4.2.3) C IV profiles are 5400–11,100 km s^{-1} (8200 km s^{-1} on average), near the broad end of the FWHM distribution.

To summarize, we caution against blindly adopting M_{BH} estimates based on any line with FWHM $\gtrsim$ 8000 km s^{-1}. For example, searching for quasars in Shen et al. (2011) with S/N > 10 and flagged not to be double-peaked emitters, there are 14 Hα-based and 213 Hβ-based masses with $M_{BH} > 10^{9.5}\,M_\odot$ at $z < 0.37$ and $z < 0.7$, respectively. However, 14/14 Hα-based and 212/213 Hβ-based objects have broad line FWHM > 8000 km s^{-1} and the spectra of these objects need to be carefully checked. Indeed, through visual inspection of the spectra, we find that 12 out of the 14 Hα spectra indicating $M_{BH} > 10^{9.5}\,M_\odot$ and FWHM > 8000 km s^{-1} show moderate to strong double-peaked line profiles, raising caution about their M_{BH} values.

5.2. M_{BH} Bias Due to C IV Blueshift

Next, we consider the general effect of blueshifted C IV on M_{BH} estimation, thought to be a combined effect of outflows and obscuration in high ionization lines (e.g., Baskin & Laor 2005). Though it is expected that optically bright type-1 AGNs are seen through minimal obscuring material, they display a moderate range of UV/optical through infrared colors (e.g., Richards et al. 2003; Jun & Im 2013). This hints that not only can the UV continuum emission be absorbed, but likewise for the broad line emission, so that the reliability of UV line widths should be checked, especially at higher levels of obscuration. We follow S12 to plot in Figure 11(a) the ratio between the C IV and Balmer broad line FWHMs against rest-frame 1350–5100 Å continuum color, using compiled references and this work. We checked that the plotted objects are luminous enough to have an estimated host galaxy contamination of less than 20% at 5100 Å (Shen et al. 2011), or have *Hubble Space Telescope* imaging so that the spatially resolved host galaxy contamination is below 20% at optical wavelengths. We do not find any correlation between the quantities (linear Pearson correlation coefficient $r = 0.18$), implying the C IV line width does not suffer any more systematic biases than the Balmer lines. Instead, having checked that the IRTF sources with blueshifted C IV emission show broader C IV than the Balmer line widths (Section 4.2), we plot in Figures 11(b) and (c) the C IV to Balmer broad line FWHM and M_{BH} ratios against the Balmer to C IV broad line shift from compiled references and from this work. We find that the quantities are positively correlated ($r = 0.66$ and 0.70 respectively), in accord with the trends between the C IV and Mg II (e.g., Shen et al. 2008). The linear fit to the data based on the FITEXY and BCES methods (Press et al. 1992; Akritas & Bershady 1996) respectively yield

$$\begin{aligned}\log(\mathrm{FWHM_{C\,IV}}/\mathrm{FWHM_{H\beta}}) &= -(0.201 \pm 0.003)\\ &\quad - (0.161 \pm 0.002)(\mathrm{v_{C\,IV}} - \mathrm{v_{H\alpha/H\beta}})(10^3\ \mathrm{km\ s^{-1}})\\ \log(\mathrm{FWHM_{C\,IV}}/\mathrm{FWHM_{H\beta}}) &= -(0.190 \pm 0.015)\\ &\quad - (0.161 \pm 0.010)(\mathrm{v_{C\,IV}} - \mathrm{v_{H\alpha/H\beta}})(10^3\ \mathrm{km\ s^{-1}}), \quad (3)\end{aligned}$$

$$\begin{aligned}\log(\mathrm{M_{BH,C\,IV}}/\mathrm{M_{BH,H\beta}}) &= -(0.457 \pm 0.006)\\ &\quad - (0.382 \pm 0.003)(\mathrm{v_{C\,IV}} - \mathrm{v_{H\alpha/H\beta}})(10^3\ \mathrm{km\ s^{-1}})\\ \log(\mathrm{M_{BH,C\,IV}}/\mathrm{M_{BH,H\beta}}) &= -(0.371 \pm 0.035)\\ &\quad - (0.335 \pm 0.022)(\mathrm{v_{C\,IV}} - \mathrm{v_{H\alpha/H\beta}})(10^3\ \mathrm{km\ s^{-1}}). \quad (4)\end{aligned}$$

Because of the tighter linear correlation for the M_{BH} ratios than the FWHM ratios, we recommend using Equation (4) when correcting the C IV M_{BH} values. Equations (3) and (4) imply that C IV to Balmer FWHM ratios systematically increase with C IV blueshift (e.g., Coatman et al. 2016, 2017, hereafter C17), for instance, by 0.32 dex between 0 and 2000 km s^{-1} C IV blueshift, or by 0.67–0.76 dex in $M_{BH,C\,IV}/M_{BH,H\beta}$ values.

The blueshift of the C IV line has been considered as one of the causes for the scatter in the broad line width ratios against Mg II or Balmer lines. At the time of writing, we find the C17 relation well points out for the systematic overestimation in C IV to Balmer line width ratios along C IV blueshift, drawing similar conclusions although linear in the correction method as

opposed to our log-linear correction. We compare the reduction in the intrinsic scatter between the C IV to Hβ $M_{\rm BH}$ ratios when applying either correction to the data in Figure 11(c), for the C IV blueshift bounded within -1000 and 5000 km s^{-1} in order to compare well sampled data and to reject data where the C17 relation diverges. We find that $\sigma_{\rm int}$ decreases merely from 0.38 to 0.27 dex (this work, FITEXY), 0.25 dex (this work, BCES), and 0.30 dex (C17 relation). The C17 relation performs as much as ours (or perhaps better at C IV blueshifts larger than 5000 km s^{-1}) to reduce the $\sigma_{\rm int}$ values, considering that we are correcting for the $M_{\rm BH}$ ratios while using the FWHM^2 ratios from C17, although the linear correlation coefficients are slightly larger between the C IV blueshift and log $M_{\rm BH}$ ratio ($r = 0.70$) than against $M_{\rm BH}$ ratio ($r = 0.66$). In any case, the relatively minor change in $\sigma_{\rm int}$ values (0.08–0.13 out of 0.38 dex) imply that the broad line outflows, although effectively explaining the bias in the C IV to Balmer $M_{\rm BH}$ ratios, are not fully responsible for the scatter.

Among other mutually correlated observables (Eigenvector 1, Boroson & Green 1992) that scale with the broad line width ratios or the residuals of the ratios are the C IV luminosity, equivalent width of the C IV line, and shape parameters (e.g., Baskin & Laor 2005; Runnoe et al. 2013), reducing the intrinsic scatter between the C IV- and Balmer-based $M_{\rm BH}$ values from 0.43–0.51 dex by merely 0.10–0.13 dex. Many Eigenvector 1 properties are correlated with the Eddington ratio, perhaps hinting that the C IV line width bias could be driven by a physical mechanism such as strong outflowing winds at high Eddington ratios, although the high Eddington ratio is a necessary rather than sufficient condition for C IV outflows (Baskin & Laor 2005). We further note that studies reporting the reduction of the $\sigma_{\rm int}$ value between the C IV- and Balmer-based $M_{\rm BH}$ values by adding an obscuration correction term or adopting a shallower scaling of the FWHM$_{\rm C IV}$ term (e.g., Assef et al. 2011; S12) are not as effective when the dynamic range and sampling of the parameter space are improved (e.g., Figure 11(a) in this work, J15). Overall, the intrinsic scatter between C IV- to Balmer-based $M_{\rm BH}$ values ($\sim$0.4 dex, J15) is not yet fully explained by either empirical or physical approaches, leaving the possibility that the C IV mass estimator is less reliable than the Balmer- or Mg II-based estimators for more fundamental reasons, e.g., non-virialized or non-reverberating velocity structure within the C IV line region (Denney 2012).

5.3. EMBH–Host Galaxy Coevolution

We probe how the observed EMBH masses in AGNs constrain models for galaxy evolution in Figure 12, showing Balmer $M_{\rm BH}$ values at the massive end as a function of redshift from compiled references and from this work. The most massive BHs seen in local inactive galaxies appear similarly massive to AGNs at $z \sim 1$ and beyond. Assuming that the EMBH hosting AGNs at $z = 2.5$ will become inactive bulge galaxies falling on the local $M_{\rm BH}$–$M_{\rm bulge}$ relation, we draw in Figure 12 the expected evolutionary tracks of the $M_{\rm bulge}$ adopting the consensus of observed and simulated evolution of σ_* and effective radius ($R_{\rm e}$) for massive galaxies, i.e., 20%–40% decrease in σ_* and 3–5 times increase in $R_{\rm e}$ from $z = 2$ to 0, and the proportionality $M_{\rm bulge} \propto R_{\rm e}\sigma_*^2$ (e.g., Trujillo et al. 2006; Toft et al. 2007; Cenarro & Trujillo 2009; Naab et al. 2009; van Dokkum et al. 2010; Oser et al. 2012; Trippe 2016). The estimated $M_{\rm bulge}$ values at $z \sim 2$ are factors of a few

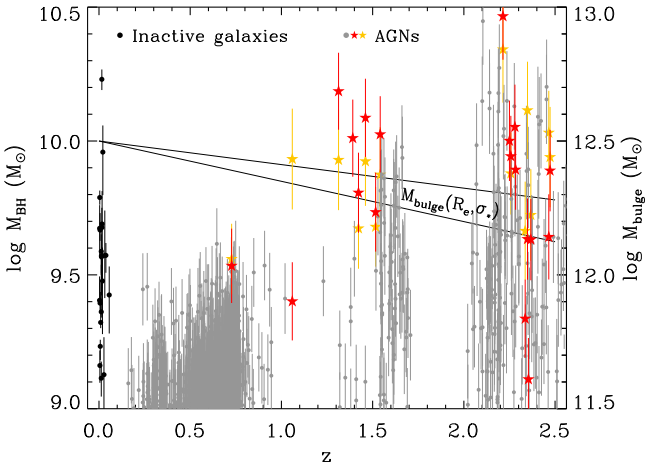

Figure 12. Massive end of the black hole distribution as a function of redshift. For active galaxies Balmer $M_{\rm BH}$ values derived using the J15 estimator are plotted. The data come from this work (stars, Hα in red and Hβ in yellow) and from the literature (both Hα and Hβ in gray, Shemmer et al. 2004; Dietrich et al. 2009; Assef et al. 2011; Shen et al. 2011; S12; Matsuoka et al. 2013; C17 and references within) converted to our adopted cosmology. Sources showing double-peaked broad emission or having broad FWHM > 8000 km s^{-1} are removed. For inactive galaxies in the local universe we plot the direct dynamical measurements (black, Rusli et al. 2011; Kormendy & Ho 2013; Walsh et al. 2015; Thomas et al. 2016). We limit the data to sources with $M_{\rm BH}$ uncertainties less than 0.2 dex, and with continuum S/N > 10 for the SDSS DR9 objects (without measurement errors for the continuum luminosity and line width, thus their $M_{\rm BH}$ errors on the figure are underestimated). The model evolution of $M_{\rm bulge}$ assuming that it will become a fiducial $10^{12.5}$ $M_\odot$ bulge galaxy hosting a 10^{10} $M_\odot$ BH at $z = 0$ (e.g., McConnell & Ma 2013) is overplotted for when using $M_{\rm bulge} \propto R_{\rm e}\sigma_*^2$ (solid line), with the range of slopes obtained from the literature (Section 5.2).

smaller than the most massive local galaxies, leaving the possibility for $M_{\rm bulge}$ to grow after the BH has reached EMBH mass. Therefore, the observed EMBH masses in $z = 1$–2 AGNs require them to be overmassive to their host bulges.

On the other hand, we consider the effect of relaxing the assumption that the most massive BHs are hosted in the most massive early-type galaxies shaping the present day BH–galaxy scaling relations. First, the host galaxies of $z = 1$–2 EMBHs may not end up being the most massive galaxies due to galaxy environment. If the EMBH hosts are not the central galaxies in moderately dense environments (e.g., Brown et al. 2008; Wellons et al. 2016), they will not encounter minor mergers as frequently, which would imply more limited size growth. Indeed, local examples of overmassive BHs are often in compact galaxies (e.g., Rusli et al. 2011; van den Bosch et al. 2012; Ferré-Mateu et al. 2015; Walsh et al. 2016). Second, it could be that the host galaxy evolves to be massive in stellar content, but not bulge-dominated in morphology. Gas-rich major mergers that could trigger the observed AGN luminosity traced by our sample (e.g., Hong et al. 2015) and form a bulge may still leave a disk, and transformation into the bulge through secular processes or repeated minor mergers could have somehow been prevented (e.g., Springel & Hernquist 2005; Robertson et al. 2006; van der Wel et al. 2011). This scenario is consistent with most of the overmassive BHs on the $M_{\rm BH}$–$M_{\rm bulge}$ relation (e.g., Walsh et al. 2016) being lenticular galaxies, with bulge to total mass (or luminosity) ratios typically ranging below unity (0.1–0.6, e.g., Cretton & van den Bosch 1999; Rusli et al. 2011; van den Bosch et al. 2012; Strader et al. 2013; Walsh et al. 2015).

We have discussed that the relative growth modes for extremely massive BHs and their host galaxies can not only depend on the galaxy mass, but also environment or morphology. Galaxy environment studies of EMBH hosts will help probe the contribution of mergers shaping the BH–galaxy scaling relations (e.g., Jahnke & Macciò 2011), and spatially resolved imaging of the host will tell if a two-parameter relation (e.g., $M_{\rm BH}$–σ_*) is sufficient to explain BH–galaxy coevolution. Luminous AGN activity is rare in the present-day universe and EMBHs have mostly been found in quiescent early-type galaxies. Further discoveries of EMBHs (e.g., van den Bosch et al. 2015) in lower bulge masses will constrain how tight the BH–galaxy scaling relations are at their massive end, and how often EMBHs in distant AGNs remain in the most massive galaxies at present.

6. Summary

We performed followup rest-optical spectrocopy of a sample of 26 extremely massive quasars at $0.7 < z < 2.5$ in order to cross-check their rest-UV $M_{\rm BH}$ values, and to examine possible biases affecting the measured $M_{\rm BH}$ values. We summarize the results as follows.

1. The rest-UV $M_{\rm BH}$ estimates of $\lesssim 10^{10}\,M_\odot$ in luminous AGNs, are generally consistent with the Balmer-based estimates. However, double-peaked emitters strongest in the Hα, extremely broad Fe II around Mg II, and highly blueshifted ($>$2000 km s^{-1}) C IV profiles are frequently associated with $M_{\rm BH} \gtrsim 10^{10}\,M_\odot$ estimates, easily boosting reported masses by a factor of a few. We find these cases mostly at broad line FWHM > 8000 km s^{-1}, and make cautionary remarks for estimating $M_{\rm BH}$ values based on any line width over this limit. The presence of broadened (FWHM > 1000 km s^{-1}) narrow emission (e.g., [O III]), however, does not appear to significantly bias EMBH mass measurements.
2. We checked for systematic biases in single-epoch $M_{\rm BH}$ estimators for AGNs with EMBH masses and general AGNs. Anisotropic radiation and the use of broad line FWHM in place of σ are not the major cause of producing false EMBH $M_{\rm BH}$ estimates for our sample. Furthermore, variability, overestimated line equivalent width from cold accretion disks, and obscuration do not bias the $M_{\rm BH}$ estimates for general type-1 quasars by more than $\sim$0.1 dex. Instead, correcting the C IV $M_{\rm BH}$ estimator based on its blueshift relative to the Balmer line redshift, the C IV $M_{\rm BH}$ values decrease by 0.67–0.76 dex from a zero to 2000 km s^{-1} blueshift, with sizable scatter.
3. Removing the systematically uncertain $M_{\rm BH}$ values arising from the spectra or mass estimators, there is still a chance that EMBH masses are boosted by anisotropic motion of the broad line region from $\sim 10^{9.5}\,M_\odot$ BHs, but this is contradictory to the current $\sigma_{\rm int}$ values of the local $M_{\rm BH}$–σ_* relation for AGNs. The observed and simulated growth of $M_{\rm bulge}$ in massive galaxies support that EMBH hosting AGNs at $z = 1$–2 are growing predominantly by minor dry mergers, with their BHs overmassive to the host's bulge mass. Depending on the galaxy environment on galactic and intergalactic scales, we expect that either the EMBH host will catch up the BH growth or the BH will stay overmassive to the bulge.

We thank the anonymous referee for the comments that greatly improved the paper, and the IRTF staff for their kind help during data acquisition at on-site and remote observations. This work was supported by the National Research Foundation of Korea (NRF) grant, No. 2008-0060544, funded by the Korea government (MSIP). This research was supported by an appointment to the NASA Postdoctoral Program at the Jet Propulsion Laboratory, administered by Universities Space Research Association under contract with NASA. H.D.J., M.I., and D.K. were visiting astronomers at the Infrared Telescope Facility, which is operated by the University of Hawaii under contract NNH14CK55B with the National Aeronautics and Space Administration. This publication makes use of data products from the Two Micron All Sky Survey, which is a joint project of the University of Massachusetts and the Infrared Processing and Analysis Center/California Institute of Technology, funded by the National Aeronautics and Space Administration and the National Science Foundation. This publication makes use of data products from the United Kingdom Infrared Deep Sky Survey. The United Kingdom Infrared Telescope (UKIRT) is supported by NASA and operated under an agreement among the University of Hawaii, the University of Arizona, and Lockheed Martin Advanced Technology Center; operations are enabled through the cooperation of the East Asian Observatory. When the data reported here were acquired, UKIRT was operated by the Joint Astronomy Centre on behalf of the Science and Technology Facilities Council of the UK This publication makes use of data products from the Wide-field Infrared Survey Explorer, which is a joint project of the University of California, Los Angeles, and the Jet Propulsion Laboratory/California Institute of Technology, funded by the National Aeronautics and Space Administration.

References

Akritas, M. G., & Bershady, M. A. 1996, ApJ, 470, 706
Alam, S., Albareti, F. D., Allende Prieto, C., et al. 2015, ApJS, 219, 12
Assef, R. J., Denney, K. D., Kochanek, C. S., et al. 2011, ApJ, 742, 93
Barth, A. J., Ho, L. C., & Sargent, W. L. W. 2002, AJ, 124, 2607
Baskin, A., & Laor, A. 2005, MNRAS, 356, 1029
Bentz, M. C., Denney, K. D., Grier, C. J., et al. 2013, ApJ, 767, 149
Bentz, M. C., Peterson, B. M., Pogge, R. W., Vestergaard, M., & Onken, C. A. 2006, ApJ, 644, 133
Blandford, R. D., & McKee, C. F. 1982, ApJ, 255, 419
Bonifacio, P., Monai, S., & Beers, T. C. 2000, AJ, 120, 2065
Boroson, T. A., & Green, R. F. 1992, ApJS, 80, 109
Brewer, B. J., Treu, T., Pancoast, A., et al. 2011, ApJL, 733, L33
Brown, M. J. I., Zheng, Z., White, M., et al. 2008, ApJ, 682, 937
Brusa, M., Bongiorno, A., Cresci, G., et al. 2015, MNRAS, 446, 2394
Cenarro, A. J., & Trujillo, I. 2009, ApJL, 696, L43
Chelouche, D., Daniel, E., & Kaspi, S. 2012, ApJL, 750, L43
Chen, K., & Halpern, J. P. 1989, ApJ, 344, 115
Coatman, L., Hewett, P. C., Banerji, M., et al. 2017, MNRAS, 465, 2120
Coatman, L., Hewett, P. C., Banerji, M., & Richards, G. T. 2016, MNRAS, 461, 647
Collin, S., Kawaguchi, T., Peterson, B. M., & Vestergaard, M. 2006, A&A, 456, 75
Cretton, N., & van den Bosch, F. C. 1999, ApJ, 514, 704
Cushing, M. C., Vacca, W. D., & Rayner, J. T. 2004, PASP, 116, 362
Denney, K. D. 2012, ApJ, 759, 44
Denney, K. D., Peterson, B. M., Dietrich, M., Vestergaard, M., & Bentz, M. C. 2009, ApJ, 692, 246
Dietrich, M., Mathur, S., Grupe, D., & Komossa, S. 2009, ApJ, 696, 1998
Dietrich, M., Peterson, B. M., Albrecht, P., et al. 1998, ApJS, 115, 185
Drake, A. J., Djorgovski, S. G., Mahabal, A., et al. 2009, ApJ, 696, 870
Emsellem, E. 2013, MNRAS, 433, 1862
Eracleous, M., & Halpern, J. P. 1993, ApJ, 409, 584
Eracleous, M., & Halpern, J. P. 1994, ApJS, 90, 1

Eracleous, M., & Halpern, J. P. 2003, ApJ, 599, 886
Eracleous, M., Halpern, J. P., Storchi-Bergmann, T., et al. 2004, in IAU Symp. 222, The Interplay of Black Holes, Stars, and ISM in Galactic Nuclei, ed. T. Storchi-Bergmann, L. C. Ho., & H. R. Schmitt (Cambridge: Cambridge Univ. Press), 29
Eracleous, M., Lewis, K. T., Halpern, J. P., et al. 2015, BAAS, 225, 303.03
Ferrarese, L., & Merritt, D. 2000, ApJL, 539, L9
Ferré-Mateu, A., Mezcua, M., Trujillo, I., Balcells, M., & van den Bosch, R. C. E. 2015, ApJ, 808, 79
Gebhardt, K., Bender, R., Bower, G., et al. 2000, ApJL, 539, L13
Greene, J. E., Peng, C. Y., & Ludwig, R. R. 2010, ApJ, 709, 937
Gültekin, K., Richstone, D. O., Gebhardt, K., et al. 2009, ApJ, 698, 198
Ho, L. C., Goldoni, P., Dong, X.-B., Greene, J. E., & Ponti, G. 2012, ApJ, 754, 11
Ho, L. C., & Kim, M. 2014, ApJ, 789, 17
Hong, J., Im, M., Kim, M., & Ho, L. C. 2015, ApJ, 804, 34
Im, M., Griffiths, R. E., & Ratnatunga, K. U. 1997, ApJ, 475, 457
Inayoshi, K., & Haiman, Z. 2016, ApJ, 828, 110
Jahnke, K., & Macciò, A. V. 2011, ApJ, 734, 92
Jun, H. D., & Im, M. 2013, ApJ, 779, 104
Jun, H. D., Im, M., Lee, H. M., et al. 2015, ApJ, 806, 109
Kaspi, S., Brandt, W. N., Maoz, D., et al. 2007, ApJ, 659, 997
Kaspi, S., Smith, P. S., Netzer, H., et al. 2000, ApJ, 533, 631
King, A. 2016, MNRAS, 456, L109
Kollatschny, W., & Zetzl, M. 2013, A&A, 549, A100
Kormendy, J., & Ho, L. C. 2013, ARA&A, 51, 511
Kormendy, J., & Richstone, D. 1995, ARA&A, 33, 581
Laor, A., Bahcall, J. N., Jannuzi, B. T., et al. 1994, ApJ, 420, 110
Laor, A., & Davis, S. W. 2011, MNRAS, 417, 681
Lawrence, A., Warren, S. J., Almaini, O., et al. 2007, MNRAS, 379, 1599
Lewis, K. T., & Eracleous, M. 2006, ApJ, 642, 711
Lewis, K. T., Eracleous, M., & Storchi-Bergmann, T. 2010, ApJS, 187, 416
Liu, G., Zakamska, N. L., & Greene, J. E. 2014, MNRAS, 442, 1303
Maoz, D., Netzer, H., Peterson, B. M., et al. 1993, ApJ, 404, 576
Markwardt, C. B. 2009, in ASP Conf. Ser. 411, Astronomical Data Analysis Software and Systems XVIII, ed. D. A. Bohlender, D. Durand, & P. Dowler (San Francisco: CA: ASP), 251
Martin, D. C., Fanson, J., Schiminovich, D., et al. 2005, ApJL, 619, L1
Marziani, P., Sulentic, J. W., Plauchu-Frayn, I., & del Olmo, A. 2013, A&A, 555, A89
Matsuoka, K., Silverman, J. D., Schramm, M., et al. 2013, ApJ, 771, 64
McConnell, N. J., & Ma, C.-P. 2013, ApJ, 764, 184
McConnell, N. J., Ma, C.-P., Gebhardt, K., et al. 2011, Natur, 480, 215
Mejía-Restrepo, J. E., Trakhtenbrot, B., Lira, P., Netzer, H., & Capellupo, D. M. 2016, MNRAS, 460, 187
Naab, T., Johansson, P. H., & Ostriker, J. P. 2009, ApJL, 699, L178
Nelson, C. H., Green, R. F., Bower, G., Gebhardt, K., & Weistrop, D. 2004, ApJ, 615, 652
Netzer, H., Lira, P., Trakhtenbrot, B., Shemmer, O., & Cury, I. 2007, ApJ, 671, 1256
Netzer, H., Shemmer, O., Maiolino, R., et al. 2004, ApJ, 614, 558
O'Brien, P. T., Dietrich, M., Leighly, K., et al. 1998, ApJ, 509, 163
Oser, L., Naab, T., Ostriker, J. P., & Johansson, P. H. 2012, ApJ, 744, 63
Pancoast, A., Brewer, B. J., Treu, T., et al. 2014, MNRAS, 445, 3073
Park, D., Woo, J.-H., Denney, K. D., & Shin, J. 2013, ApJ, 770, 87
Park, D., Woo, J.-H., Treu, T., et al. 2012, ApJ, 747, 30
Peterson, B. M. 1993, PASP, 105, 247
Peterson, B. M., Ferrarese, L., Gilbert, K. M., et al. 2004, ApJ, 613, 682
Press, W. H., Teukolsky, S. A., Vetterling, W. T., & Flannery, B. P. 1992, Numerical Recipes in C: The Art of Scientific Computing (2nd ed.; Cambridge: Cambridge Univ. Press)
Rayner, J. T., Toomey, D. W., Onaka, P. M., et al. 2003, PASP, 115, 362
Richards, G. T., Hall, P. B., Vanden Berk, D. E., et al. 2003, AJ, 126, 1131
Richards, G. T., Lacy, M., Storrie-Lombardi, L. J., et al. 2006a, ApJS, 166, 470
Richards, G. T., Vanden Berk, D. E., Reichard, T. A., et al. 2002, AJ, 124, 1
Robertson, B., Bullock, J. S., Cox, T. J., et al. 2006, ApJ, 645, 986
Runnoe, J. C., Brotherton, M. S., Shang, Z., & DiPompeo, M. A. 2013, MNRAS, 434, 848
Rusli, S. P., Thomas, J., Erwin, P., et al. 2011, MNRAS, 410, 1223
Savorgnan, G. A. D., & Graham, A. W. 2016, MNRAS, 457, 320
Schlegel, D. J., Finkbeiner, D. P., & Davis, M. 1998, ApJ, 500, 525
Schneider, D. P., Richards, G. T., Hall, P. B., et al. 2010, AJ, 139, 2360
Sergeev, S. G., Pronik, V. I., Peterson, B. M., Sergeeva, E. A., & Zheng, W. 2002, ApJ, 576, 660
Seth, A. C., van den Bosch, R., Mieske, S., et al. 2014, Natur, 513, 398
Shang, Z., Wills, B. J., Wills, D., & Brotherton, M. S. 2007, AJ, 134, 294
Shemmer, O., Netzer, H., Maiolino, R., et al. 2004, ApJ, 614, 547
Shen, Y. 2016, ApJ, 817, 55
Shen, Y., Greene, J. E., Strauss, M. A., Richards, G. T., & Schneider, D. P. 2008, ApJ, 680, 169
Shen, Y., & Ho, L. C. 2014, Natur, 513, 210
Shen, Y., & Liu, X. 2012, ApJ, 753, 125
Shen, Y., Richards, G. T., Strauss, M. A., et al. 2011, ApJS, 194, 45
Skrutskie, M. F., Cutri, R. M., Stiening, R., et al. 2006, AJ, 131, 1163
Sluse, D., Schmidt, R., Courbin, F., et al. 2011, A&A, 528, A100
Springel, V., & Hernquist, L. 2005, ApJL, 622, L9
Strader, J., Seth, A. C., Forbes, D. A., et al. 2013, ApJL, 775, L6
Strateva, I. V., Strauss, M. A., Hao, L., et al. 2003, AJ, 126, 1720
Thomas, J., Ma, C.-P., McConnell, N. J., et al. 2016, Natur, 532, 340
Toft, S., van Dokkum, P., Franx, M., et al. 2007, ApJ, 671, 285
Trippe, S. 2016, JKAS, 49, 193
Trujillo, I., Förster Schreiber, N. M., Rudnick, G., et al. 2006, ApJ, 650, 18
Tsuzuki, Y., Kawara, K., Yoshii, Y., et al. 2006, ApJ, 650, 57
Vacca, W. D., Cushing, M. C., & Rayner, J. T. 2003, PASP, 115, 389
van den Bosch, R. C. E., Gebhardt, K., Gültekin, K., et al. 2012, Natur, 491, 729
van den Bosch, R. C. E., Gebhardt, K., Gültekin, K., Yıldırım, A., & Walsh, J. L. 2015, ApJS, 218, 10
van der Wel, A., Rix, H.-W., Wuyts, S., et al. 2011, ApJ, 730, 38
van Dokkum, P. G., Whitaker, K. E., Brammer, G., et al. 2010, ApJ, 709, 1018
Vanden Berk, D. E., Richards, G. T., Bauer, A., et al. 2001, AJ, 122, 549
Vestergaard, M., & Peterson, B. M. 2006, ApJ, 641, 689
Vestergaard, M., & Wilkes, B. J. 2001, ApJS, 134, 1
Volonteri, M., & Ciotti, L. 2013, ApJ, 768, 29
Walsh, J. L., van den Bosch, R. C. E., Gebhardt, K., et al. 2015, ApJ, 808, 183
Walsh, J. L., van den Bosch, R. C. E., Gebhardt, K., et al. 2016, ApJ, 817, 2
Wang, J.-G., Dong, X.-B., Wang, T.-G., et al. 2009, ApJ, 707, 1334
Wang, J.-M., Du, P., Li, Y.-R., et al. 2014, ApJL, 792, L13
Wellons, S., Torrey, P., Ma, C.-P., et al. 2016, MNRAS, 456, 1030
Woo, J.-H., Schulze, A., Park, D., et al. 2013, ApJ, 772, 49
Wright, E. L., Eisenhardt, P. R. M., Mainzer, A. K., et al. 2010, AJ, 140, 1868
Wu, X.-B., & Liu, F. K. 2004, ApJ, 614, 91
Wu, X.-B., Wang, F., Fan, X., et al. 2015, Natur, 518, 512
Zakamska, N. L., & Greene, J. E. 2014, MNRAS, 442, 784
Zhang, X.-G., Dultzin-Hacyan, D., & Wang, T.-G. 2007, MNRAS, 376, 1335